Multiscale modeling of the elastic moduli of CNT-reinforced polymers and fitting of efficiency parameters for the use of the extended rule-of-mixtures

Enrique García-Macías[a,*], Carlos Felipe Guzmán[b], Erick I. Saavedra Flores[b], Rafael Castro-Triguero[c]

[a]*Escuela Técnica Superior de Ingeniería, Universidad de Sevilla, Camino de los Descubrimientos s/n , Sevilla E-41092, Spain.*
[b]*Departamento de Ingeniería en Obras Civiles, Universidad de Santiago de Chile, Av. Ecuador 3659, Santiago, Chile*
[c]*Department of Mechanics, University of Cordoba, Campus de Rabanales, Cordoba, CP 14071, Spain*

Highlights

- An atomistic-based FEM is used in conjunction with a micromechanics approach
- Analytical and numerical micromechanics approaches are compared
- The elastic moduli of equivalent fibers are provided for numerous SWCNTs and MWCNTs
- Efficiency parameters have been fitted by polynomial expressions

Abstract

In this work, a bottom-up multiscale modeling approach is developed to estimate the effective elastic moduli of Carbon NanoTube (CNT)-reinforced polymer composites. The homogenization process comprises two successive steps, including an atomistic-based computational model and a micromechanics approach at the nano- and micro-scales, respectively. Firstly, the atomistic-based finite element model defines a cylindrical Representative Volume Element (RVE) that accounts for a carbon nanotube, the immediately surrounding matrix, and the CNT/polymer interface. The carbon-carbon bonds of the CNT are modeled using Timoshenko beams, whilst three-dimensional solid elements are used for the surrounding matrix. Through the application of four loading conditions, the RVEs are homogenized into transversely isotropic equivalent fibers by equating the associated strain energies. Secondly, the equivalent fibers are employed in a micromechanics approach to estimate the macroscopic response of non-dilute composites. This is performed using both the analytical Mori-Tanaka model and a computational RVE model with a hexagonal packing geometry. A wide spectrum of single- and multi-walled carbon nanotubes are studied, as well as two different polymeric matrices. Furthermore, the so-called efficiency parameters, imperative for the application of the simplified extended rule of mixtures, are characterized by polynomial expressions for practical filler contents. Finally, detailed parametric analyses are also provided to give insight into the sensitivity of the macroscopic response of CNT-reinforced polymer composites to microstructural features such as filler volume fraction, chirality or aspect ratio.

Keywords: Atomistic-based continuum, Carbon nanotube, Micromechanics, Mori-Tanaka method, Multiscale modeling

1. Introduction

Carbon NanoTubes (CNTs) have attracted widespread attention from the scientific community since its discovery in the '90s [1]. Due to their exceptional mechanical and physical properties, as well as their high aspect ratio and low mass density [2–5], very low filler dosages provide outstanding improvements in the overall response of CNT-based composites. Moreover, CNTs also exhibit remarkable electrical and self-sensing properties [6], which open a vast spectrum of applications for the development of multi-functional and smart composites [7–9]. Hence, accurate quantification of the material properties of CNT-reinforced composites is of pivotal importance for their design and optimization. Notwithstanding many efforts have been made from experimentation, today, the synthesis of CNT nanocomposites demands the use of complex processing methods and sophisticated testing equipment, what results in exorbitant costs [10]. Conversely, computational modeling offers a flexible and efficient alternative for predicting the properties of CNT/polymer composites and assisting their design [11, 12].

*Corresponding author.
Email address: egarcia28@us.es (Enrique García-Macías)

The mechanical and physical properties of CNTs primarily depend upon the tube chirality, which determines their atomic structure. Accordingly, CNT structures are categorized into three types according to their chirality: armchair, zig-zag or chiral [13]. Further, depending on the number of concentric tubes, CNTs are classified into Single-Walled CNTs (SWCNTs) or Multi-Walled CNTs (MWCNTs). On the other hand, when embedded into polymer matrices, the stiffening efficiency of CNTs highly depends upon the load-transfer mechanism between fillers and matrix at interfaces. The atomic interaction between CNTs and polymer chains takes place through weakly non-bonded van der Waals (vdW) and electrostatic forces [14]. Hence, an appropriate simulation technique must thoroughly capture the atomic structure of the CNTs, as well as the load transfer mechanisms at the CNT/polymer interfaces [15]. In this regard, the homogenization process is, in essence, a multi-scale problem where the atomic information must be scaled up to the macro-scale.

With regard to the modeling of CNT-reinforced composites at the atomic level, the most common approaches are [16]: (i) quantum-mechanical models, including Molecular Dynamics (MD) simulations, first-principle quantum-mechanical methods, and Monte Carlo simulations; (ii) Continuum modeling; and (iii) atomistic-based continuum modeling. In recent years, MD simulations have been extensively used to predict the physical properties of bulk systems [17]. It is worth noting the work by Frankland *et al.* [18] who conducted MD simulations to calculate the longitudinal and transverse Young's moduli of polymer nanocomposites loaded with both long and short CNTs. Similarly, Griebel and Hamaekers [19] estimated the elastic moduli of SWCNT/Polyethylene composites. MD simulations were also used by Crujicic *et al.* [20] to investigate the effect of chemical functionalization on the mechanical properties of MWCNT-vinyl ester epoxy composites. Although MD simulations can provide an important insight into many engineering problems, only systems with a limited number of atoms can be simulated, because more realistic systems entail unaffordable computational demands. With regard to continuum mechanics-based models, the major hypothesis in these theories is that CNTs can be modeled as continuum structures, including beams, shells or solids, with continuous distributions of mass and stiffness. Nonetheless, the validity of these approaches is questionable since the concepts of conventional continuum mechanics are no longer valid at the nanoscale [21]. Finally, atomistic-based continuum techniques combine the advantages of both continuum mechanics and atomistic modeling. Through appropriate relations between the interatomic potentials and the stiffness of certain continuum structures such as truss rods or link elements, it is possible to describe the atomistic structure within a continuum framework and, therefore, with moderate computational costs [22, 23].

In general, composites doped with nano-inclusions should be studied within a multiscale framework. That is, inclusions are first defined at the atomic level, then these properties condition the microstructure and, eventually, the latter determines the macroscopic behavior. It is therefore necessary to connect the above-mentioned atomistic frameworks with a micromechanics approach, along with an appropriate upscaling rule. To this aim, a common practice is to define equivalent representative micro-inclusions that account for the details of the atomic structure [18, 19, 24–26]. In this line, a noteworthy contribution was done by Yang *et al.* [27] who developed a multiscale model consisting of MD simulations and a modified multi-inclusion micromechanics approach. In that way, those authors investigated the CNT size effect and weakened bonding effect at interfaces on the macroscopic stiffness of CNT/polymer composites. Wernik and Meguid [24] proposed a multiscale approach based on the combination of an atomistic-based continuum model, the Mori-Tanaka model and an hybrid Monte Carlo Finite Element model.

These multiscale approaches require complex calculations and a deep understanding of the mechanics of the problem, what hinders their practical application. For this reason, it would be desirable to count on simplified homogenization approaches, accurate enough for preliminary design purposes. In line with this idea, an increasing number of recent publications in the realm of CNT nanocomposites have been conducted by the Extended Rule of Mixtures (EROM) [28–32]. The EROM is based upon a modification of the classical Voigt and Reuss bounds by the so-termed efficiency parameters [33]. The accuracy of this model is determined by these parameters, which must be fitted from experiments or more complex multi-scale simulations. Unfortunately, phenomenological or regressive definitions of the efficiency parameters as functions of the filler content for certain composites are still lacking in the literature, a fact that limits the applicability of the EROM.

In this paper, a multiscale homogenization approach is developed for the study of CNT-reinforced polymer composites. In particular, the present approach combines an atomistic-based continuum model with two different micromechanics approaches, including the analytical Mori-Tanaka model and a Finite Element (FE) RVE model with periodic hexagonal arrangement of fibers. Firstly, the atomistic-based model defines an FE cylindrical RVE that accounts for the atomic structure of a CNT, the surrounding polymer matrix, and the CNT/polymer interface. Through the application of four loading conditions, the cylindrical RVEs are homogenized into transversely isotropic representative fibers with equivalent strain energies. Secondly, the equivalent fibers are utilized as micro-inclusions in a micromechanics approach in order to estimate the macroscopic response of non-dilute composites. A wide spectrum of single- and multi-walled CNTs are studied, as well as two different polymeric matrices. The results are compared against previously published results in the open literature to demonstrate the validity of the developed approach. Furthermore, the numerical results are aimed at addressing the above-mentioned gap in the

literature on analytical expressions for the efficiency parameters to be used in the simplified EROM. Specifically, very simple polynomial expressions are fitted for a wide range of filler contents and CNT chiralities. Finally, detailed parametric analyses are also provided to give insight into the sensitivity of the macroscopic response of CNT/polymer composites to the CNT volume fraction, chirality, and aspect ratio.

The paper is organized as follows: Section 2 introduces the proposed multiscale micromechanical framework. Within this section, Subsection 2.1 overviews the atomistic-based continuum technique to analyze CNT-reinforced polymers at the nano-scale, and Subsection 2.2 overviews the upscaling techniques from micro to macro scales. Section 3 presents the numerical results and discussion and, finally, Section 4 concludes this paper. Throughout the text, a boldface letter stands for a fourth-order tensor, $\mathbf{A} \equiv A_{ijkl}$, while a colon between two tensors represents the inner product, $\mathbf{A} : \mathbf{B} \equiv A_{ijkl}B_{klmn}$.

2. Multiscale model of CNT-reinforced composites

In this section, a bottom-up multiscale model is developed in three consecutive steps. Firstly, the CNT/polymer interaction is studied at the nano-scale by an FE atomistic-based RVE. The RVE consists of a carbon nanotube, the immediately surrounding polymer matrix, and the CNT/polymer interphase. Secondly, the RVE is converted into a homogenized continuous representative fiber. Finally, considering the equivalent fibers as micro-inclusions and the polymer as the matrix phase, the macroscopic properties of the nanocomposite are computed using a micromechanics framework. Fig. 1 schematically illustrates the steps involved in the multiscale model. Each step is described in the following sections.

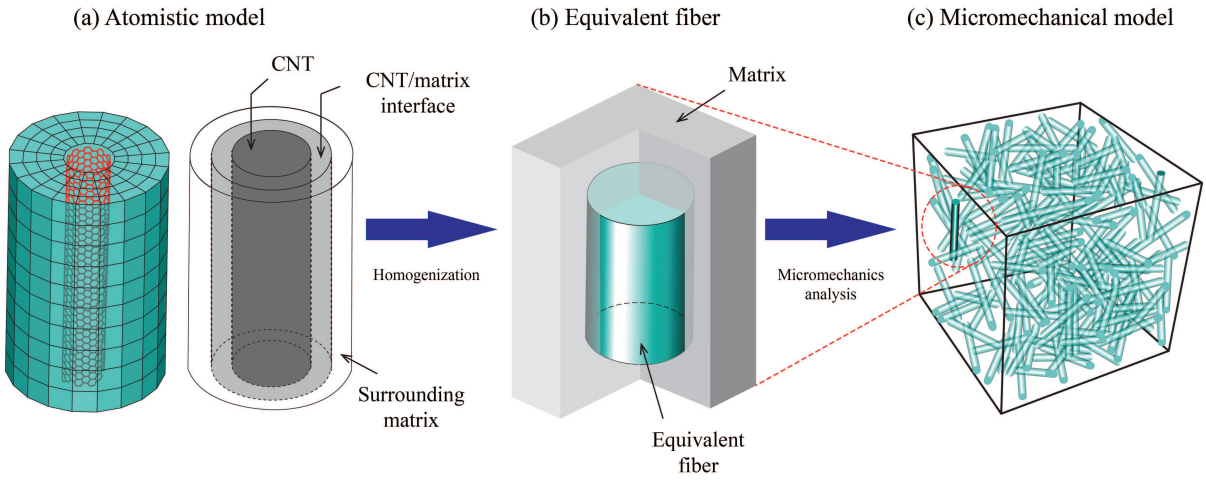

Figure 1: Schematic diagram of the analysis procedure to scale-up the elastic properties of CNT nano-reinforced polymer composites to the macroscale.

2.1. FE atomistic-based modeling

The first RVE is defined at the nano-scale and accounts for the interaction between CNTs and the surrounding polymer matrix, as sketched in Fig. 1(a). The modeling of CNTs follows the lattice approach developed by Li and Chou [34]. This approach assumes that the carbon atoms and their interaction within the nanotube can be represented as a frame-like structure. Thus, the bonds among neighboring atoms can be assumed to behave like structural beam elements in a FE framework. The methodology is based on a linkage between the chemistry of the bonds and the structural mechanics of the beam elements. This is done by linking interatomic potential energies to the strain energies of an equivalent beam element representing the carbon-carbon (C-C) bond. Hence, the potential energy of the system, consisting of the force field existing among atomic nuclei, can be represented as [35]:

$$U = \underbrace{\sum U_r + \sum U_\theta + \sum U_\phi + \sum U_\omega}_{\text{bonded}} + \underbrace{\sum U_{\text{vdW}} + \sum U_{\text{el}}}_{\text{non-bonded}} \tag{1}$$

where U_r is the potential energy associated with bond stretching, U_θ with bond angle bending, U_ϕ with bond dihedral angle torsion and U_ω with out-of-plane bending. U_{vdW} and U_{el} are the potential energies of non-bonded interactions, representing the vdW forces and the electromagnetic interactions, respectively. Assuming linear elastic behavior, a direct relation between the sectional stiffness of the beam element and the force constant in molecular mechanics can be established [34]:

$$\frac{EA}{L} = k_r, \quad \frac{EI}{L} = k_\theta, \quad \frac{GJ}{L} = k_\tau \tag{2}$$

with:

$$A = \frac{\pi d^2}{4}, \quad I = \frac{\pi d^4}{64}, \quad G = \frac{\pi d^4}{32} \tag{3}$$

where d is the beam element (bond) diameter, E is the Young's modulus, A is the transversal area of the beam element, L is the beam element length, I is the second moment of area, G is the shear modulus and J is the polar second moment of area. The C-C bond length is considered to be $L \approx 0.141$ nm [34]. k_r, k_θ and k_τ stand for the bond force constants for stretching, bending and torsion, respectively. Assuming a circular cross section, it is possible to obtain:

$$d = 4\sqrt{\frac{k_\theta}{k_r}}, \quad E = \frac{k_r L}{A}, \quad G = \frac{k_s L}{J}, \quad \nu = \frac{E}{2G} - 1 \tag{4}$$

where ν is the Poisson's ratio. In the literature, different values of the force constants are available. In this paper, the selected parameters are $K_s = 973.33\,\text{nN nm}^{-1}$, $K_\theta = 1.390\,\text{nN nm rad}^{-2}$ and $K_\tau = 0.2788\,\text{nN nm rad}^{-2}$ [36]. The constants are tuned after calculation of the commonly accepted value of the Young's modulus of graphene sheets ($\approx$1.02 TPa-1.06 TPa) [37].

2.1.1. Isolated CNTs

All the simulations are performed using the commercial FE software ANSYS [38]. The CNT is represented as a frame of beam elements. For this purpose, the 3D 2-node `BEAM188` element is used. This element is based on the Timoshenko beam theory, including shear deformation effects. The cross section is assumed to be rigid and circular, with a linear shape function along the length of the element.

A SWCNT can be considered as a rolled-up graphene sheet. The interaction among nodes is then given only by the covalent bond between neighboring atoms, here represented as a a beam element between two nodes. Fig. 2 (a) shows the FE mesh of a SWCNT.

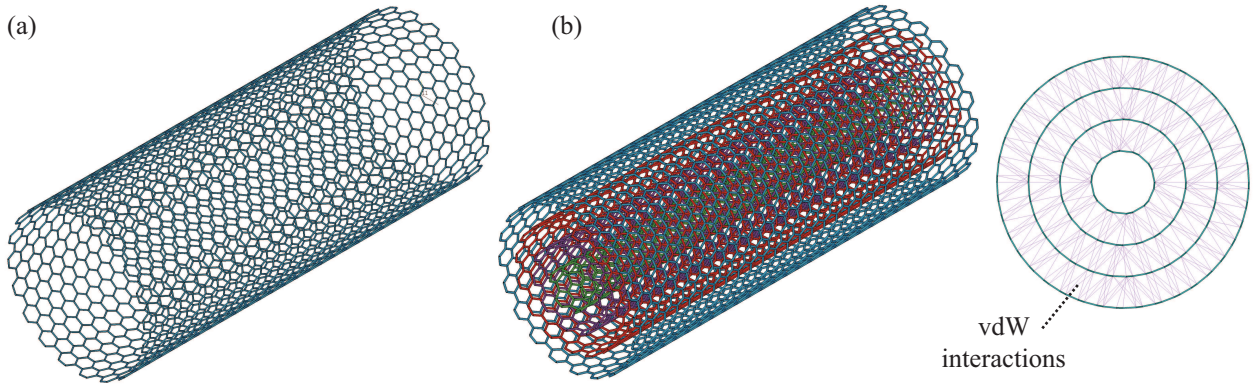

Figure 2: SWCNT (a) and MWCNT with four layers (b).

On the other hand, MWCNTs consist of several rolled-up graphene sheets forming concentric tubes, each of them connected through vdW interactions. Fig. 2(b) shows the FE mesh of a MWCNT. This interaction is often represented in terms of the Lennard-Jones (LJ) potential [39], whose expression reads:

$$U(r) = 4\epsilon\left[\left(\frac{\sigma}{r}\right)^{12} - \left(\frac{\sigma}{r}\right)^{6}\right] \tag{5}$$

where r is the distance between atoms. ϵ and σ are constant parameters which for the case of carbon atoms are $\epsilon = 0.0556\,\text{kcal/mol}$ and $\sigma = 0.34\,\text{nm}$. The LJ potential implies that the vdW forces are nonlinear respect to the distance. To simplify the FE analysis, two assumptions are proposed:

- The analysis is given in the small deformation (linear) range. Hence, the vdW forces are represented using a linear actuator (`LINK11` element in the ANSYS library).

- The potential (and the force arising from it) is omitted after a certain distance. After performing several simulations, the numerical results have shown that a cutoff value of 1.0σ provides good predictions on Young's moduli. That is, `LINK11` elements are defined between nodes that are located at a distance $< 1.0\sigma$.

The spring stiffness is taken as k_w =0.051 89 TPa, value taken from Fan *et al.* [40] and adapted to be proportional to the Young's modulus used in this paper. Also, the RVEs are defined with a filler length of 10 nm.

2.1.2. Polymer matrix modeling

Once the CNT is modeled, the immediately surrounding polymer matrix must be also included along with the interactions at the interface. To this aim, the matrix material is modeled using 3D `SOLID185` elements as shown in Fig. 3 (a). The thickness of the surrounding polymer matrix has been selected to be equal to 1 nm. The CNT interacts with the polymer through vdW forces. Therefore, the interphase is modeled in the same fashion as for MWCNTs in Section 2.1.1, as shown in Fig. 3 (b).

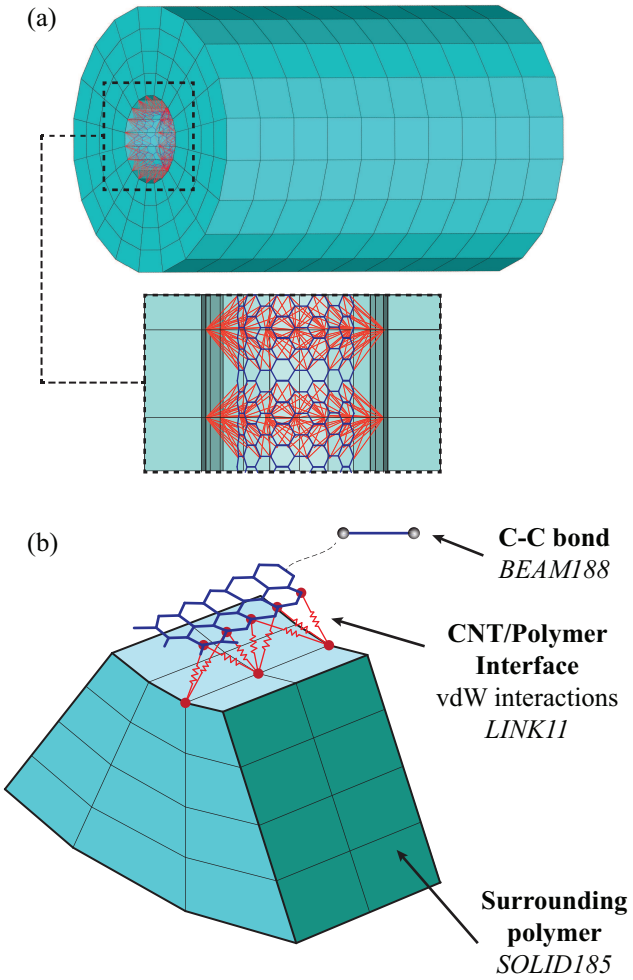

Figure 3: Perspective view of the FE mesh (a) and schematic representation of the modeling of CNT/polymer vdW interactions (b).

2.1.3. Representative equivalent fiber

After developing the atomistic-based continuum structure, it is possible to homogenize the RVE into a representative fiber. The resulting fiber, which has the same cylindrical geometry as the RVE, is assumed linearly elastic, homogeneous and continuous. Due to the particular atomic structure of CNTs, equivalent fibers are typically assumed transversely isotropic and, therefore, certain loads and boundary conditions have to be applied so that five independent material parameters are obtained: the longitudinal Young modulus E_{11}, the Poisson ratio ν_{12}, the shear modulus G_{12} and the bulk modulus K_{23}. To obtain these parameters, four loading conditions are applied [10]: uniaxial tension (to obtain E_{11} and ν_{12}), torsion (G_{12}) and hydrostatic pressure (K_{23}). The displacements and fixations are applied to the nodes at both ends of the CNT, except in the hydrostatic case where the displacement

is applied in the radial direction of the entire surface of the cylinder without the caps. The boundary conditions are shown in Fig. 4.

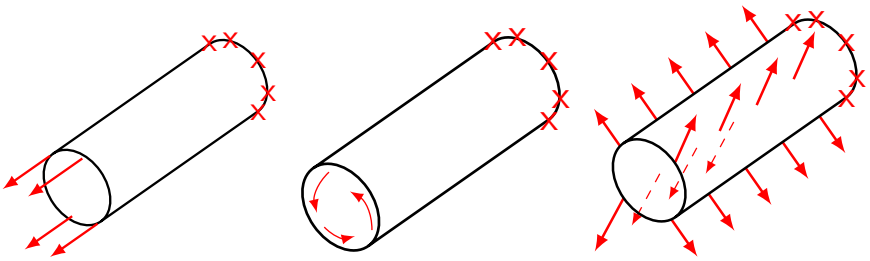

(a) Uniaxial tension. (b) Torsion. (c) Hydrostatic pressure.

Figure 4: Boundary conditions applied to CNTs.

Afterwards, the mechanical properties of the equivalent fiber can be determined by equating its total strain energy to that of the atomistic-based continuum structure. In the lattice approach, the Young's modulus is calculated in a classical way:

$$E_{11} = \frac{\sigma_{11}}{\epsilon_{11}} = \frac{F_{11} L_c}{A_t \Delta L_c} \tag{6}$$

where L_c is the length of the CNT and ΔL_c is the tube stretching. A_t is the transversal area of the CNT, which is determined by:

$$A_t = \frac{\pi}{4}\left[(d_o + t)^2 - (d_i - t)^2\right] \tag{7}$$

with d_o and d_i being the outer and inner tube diameter measured from the tube center, respectively, as shown in Fig. 5.

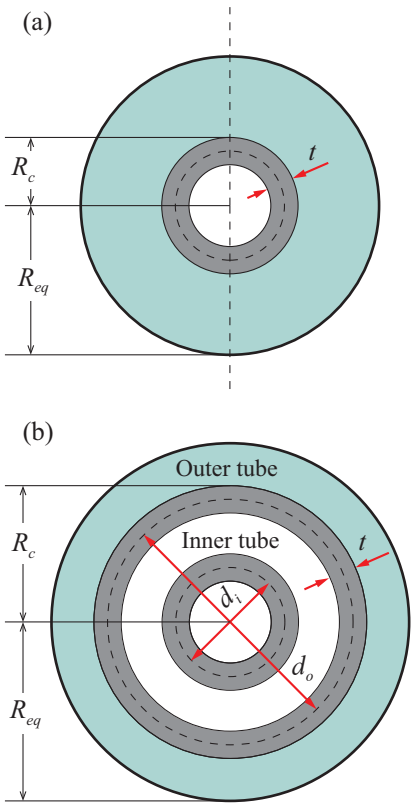

Figure 5: Geometric properties of equivalent fibers for SWCNTs (a) and MWCNTs (b).

In addition, we assume that $G_{23} = G_{13} = G_{12}$. The rest of the other effective mechanical properties are defined as follows:

$$E_{22} = \left((4K_{23})^{-1} + (4G_{23})^{-1} + \frac{\nu_{12}^2}{E_{11}} \right)^{-1} \tag{8}$$

$$\nu_{23} = \frac{E_{22}}{2G_{23}} - 1, \quad \nu_{21} = \frac{E_{22}\nu_{12}}{E_{11}} \tag{9}$$

Once the elastic moduli of the equivalent fibers are determined, the macroscopic properties of the nanocomposite can be estimated by means of a micromechanics approach. Here, the equivalent fibers account for the CNT/polymer interfacial interaction at the nanoscale, what provides a bridge to the continuum model. It is important to relate the CNT volume fraction f_r to the volume fraction of equivalent fibers f_{eq}. According to Fig. 5, both concentrations can be linked as $f_{\text{eq}} = k_f f_r$, with k_f being a transformation parameter defined as the ratio between the volume of the equivalent fiber V_{eq} and the volume of CNT, V_{CNT}. Defining R_{eq} and R_{CNT} as the radii of the equivalent fiber and the CNT (see Fig. 5), the parameter k_f can be expressed as:

$$k_f = \frac{V_{\text{eq}}}{V_{\text{CNT}}} = \left(\frac{R_{\text{eq}}}{R_{\text{CNT}}} \right)^2 \tag{10}$$

In accordance with the notation of Hill [41], the tensor of elastic moduli of equivalent fibers, $\mathbf{C}_f$, can be written as $\mathbf{C}_f = (2k_r, l_r, n_r, 2m_r, 2p_r)$, where k_r, l_r, m_r, n_r and p_r are the so-termed Hill's elastic moduli; k_r is the plane-strain bulk modulus normal to the fiber direction, n_r is the uniaxial tension modulus in the fiber direction, l_r is the associated cross modulus, m_r and p_r are the shear moduli in planes normal and parallel to the fiber direction, respectively. Hence, the constitutive tensor for the equivalent fibers (with x_3 being the axis of material symmetry) can be written in matrix notation as follows [41]:

$$\mathbf{C}_f = \begin{bmatrix} k_r + m_r & k_r - m_r & l_r & 0 & 0 & 0 \\ k_r - m_r & k_r + m_r & l_r & 0 & 0 & 0 \\ l_r & l_r & n_r & 0 & 0 & 0 \\ 0 & 0 & 0 & p_r & 0 & 0 \\ 0 & 0 & 0 & 0 & p_r & 0 \\ 0 & 0 & 0 & 0 & 0 & m_r \end{bmatrix} \tag{11}$$

where the Hill's constants of the effective fiber can be related to the engineering constants as follows [42]:

$$k_r = \frac{E_{22}}{2\left(-2\nu_{12}\nu_{21} - \nu_{23} + 1\right)}, \quad l_r = \frac{\nu_{12}E_{22}}{-2\nu_{12}\nu_{21} - \nu_{23} + 1}, \tag{12}$$

$$n_r = \frac{E_{11}\left(1 - \nu_{23}\right)}{-2\nu_{12}\nu_{21} - \nu_{23} + 1}, \quad m_r = G_{23}, \quad p_r = G_{12} \tag{13}$$

2.2. Micromechanics modeling

With the effective properties of the representative fibers, the macroscopic properties of the composites can be computed using micromechanics approaches. In this case, the equivalent fibers and the remaining matrix (i.e. the matrix outside the equivalent fibers) are considered as reinforcing and matrix phases, respectively. In this section, three different approaches are considered, namely the Mori-Tanaka mean-field homogenization approach, the EROM and a computational RVE model.

2.2.1. Mori-Tanaka model

The Mori-Tanaka (MT) model [43] allows the study of multiphase composites with microstructural considerations, such as the geometry of the inclusions, within an analytical framework. The MT model extends the theory of Eshelby [44], restricted to one single inclusion embedded in a semi-infinite elastic, homogeneous and isotropic medium, to the case of multiple inhomogeneities. The Eshelby's equivalent inclusion method [44] showed that the strain concentration tensor for the limit case of a single anisotropic ellipsoidal inhomogeneity in an infinite matrix, $\mathbf{A}^{\text{dil}}$, reads:

$$\mathbf{A}^{\text{dil}} = \left[\mathbf{I} + \mathbf{S} : \mathbf{C}_m^{-1} : \left(\mathbf{C}_f - \mathbf{C}_m \right) \right]^{-1} \tag{14}$$

where $\mathbf{I}$ is the fourth-order identity tensor, $\mathbf{C}_m$ is the constitutive tensor of the matrix, and $\mathbf{S}$ is the Eshelby's tensor, well documented in Mura [45]. Then, at non-dilute volumetric fiber concentrations, the effective elastic tensor by the MT model can be written according to Benveniste's revision [46] as:

$$\mathbf{C} = \mathbf{C}_m + f_{\text{eq}} \left\langle \left(\mathbf{C}_f - \mathbf{C}_m \right) : \mathbf{A} \right\rangle \tag{15}$$

with the mechanical strain concentration tensor $\mathbf{A}$:

$$\mathbf{A} = \mathbf{A}^{\text{dil}} : \left[(1 - f_{\text{eq}})\mathbf{I} + f_{\text{eq}} \left\langle \mathbf{A}^{\text{dil}} \right\rangle\right]^{-1} \tag{16}$$

where terms in angle brackets $\langle\cdot\rangle$ represent orientational average. Hence, the MT model also allows the analysis of different fillers arrangements, such as fully aligned or misoriented filler configurations. In order to describe the orientation of the fillers, a local coordinate system $\mathrm{K}' \equiv \left\{0; x_1' x_2' x_3'\right\}$ is set up for each fiber as indicated in Fig. 6. In order to describe the relative orientation of any inclusion and, thus, the orientation of the basis vectors, two Euler angles, θ and ψ, are required. Hence, a tensor $\mathbf{P}'$ in the local coordinate system K' can be expressed in the global coordinate system through the direction cosines g_{ij} as follows:

$$P_{ijlk} = g_{ip} g_{jq} g_{kr} g_{ls} P'_{pqrs} \tag{17}$$

The probability of a fiber lying in an infinitesimal range of angles $[\theta, \theta + \mathrm{d}\theta]$ and $[\psi, \psi + \mathrm{d}\psi]$, is defined as $\Omega(\theta, \psi) \sin(\theta) \mathrm{d}\theta \mathrm{d}\psi$, with $\Omega(\theta, \psi)$ being the so-termed Orientation Distribution Function (ODF). The integration of any ODF weighted function $F(\theta, \psi)$ over all possible orientations in the Euler space, also referred to as the orientational average of F, $\langle F \rangle$, is defined through:

$$\langle F \rangle = \int_0^{2\pi} \int_0^{\pi/2} F(\theta, \psi) \Omega(\theta, \psi) \sin(\theta) \mathrm{d}\theta \mathrm{d}\psi \tag{18}$$

Let us note that the ODF must fulfill the normalization condition, that is:

$$\int_0^{2\pi} \int_0^{\pi/2} \Omega(\theta, \psi) \sin(\theta) \mathrm{d}\theta \mathrm{d}\psi = 1 \tag{19}$$

Hence, in the case of randomly filler arrangements, the ODF is constant and of value $\Omega(\theta, \psi) = 1/2\pi$.

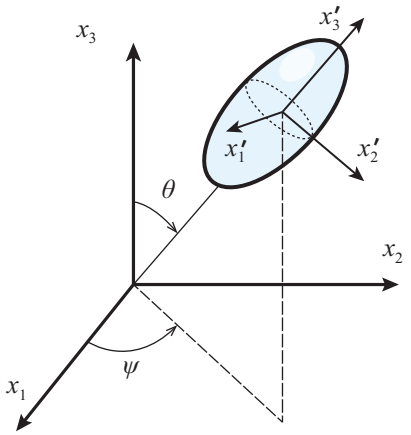

Figure 6: Euler angles defining the relation between the orientation of an ellipsoidal inclusion in the local coordinate system, $\mathrm{K}' \equiv \left\{0; x_1' x_2' x_3'\right\}$ and the global coordinate system, K≡ $\{0; x_1 x_2 x_3\}$.

2.2.2. Extended Rule of Mixtures (EROM)

The classical Rule of Mixtures (ROM) corresponds to the theoretical Reuss-Voigt bounds. In essence, this approach is a volume weighted mean of the elastic moduli of the different constituents of the composite. In spite of the fact that the ROM does not account for the particular geometry of the inclusions, nor any particle interaction or interface effects, it remains of practical interest for structural engineers due to its simplicity. In order to enhance the accuracy of the estimates, an Extended Rule of Mixtures (EROM) may be utilized for fully aligned infinite long CNT-reinforced composites as follows [33]:

$$E_{11} = \eta_1 f_r E_{11}^{\text{CNT}} + (1 - f_r) E^m \tag{20a}$$

$$\frac{\eta_2}{E_{22}} = \frac{f_r}{E_{22}^{\text{CNT}}} + \frac{1 - f_r}{E^m} \tag{20b}$$

$$\frac{\eta_3}{G_{12}} = \frac{f_r}{G_{12}^{\text{CNT}}} + \frac{1 - f_r}{G^m} \tag{20c}$$

where E_{11}^{CNT}, E_{22}^{CNT} and G_{12}^{CNT} stand for the Young's moduli and shear modulus of the isolated CNTs, respectively. E^m and G^m denote the corresponding properties of the isotropic matrix. In this model, the level of accuracy crucially depends on the so-termed CNT efficiency parameters, η_j ($j = 1, 2, 3$). The efficiency parameters have to be fitted by results obtained from experimentation or more sophisticated homogenization approaches. In this regard, some values of η_j are provided in the literature for certain composites and filler contents. However, analytical expressions for the efficiency parameters as functions of the CNT volume fraction are still not widely available in the literature.

Finally, the EROM can be also used to estimate the Young's modulus of composites doped with randomly oriented fillers using the expression proposed by Van Es [47]:

$$E_{\mathrm{random}} = 0.184E_{11} + 0.816E_{22} \tag{21}$$

2.2.3. *Computational RVE model*

The macroscopic properties of polymer composites doped with perfectly aligned fibers can be estimated by computational homogenization in a 3D RVE model with hexagonal filler arrangement. The model is developed in the FE software ANSYS [38], using the three-dimensional structural solid element `SOLID185`. As illustrated in Fig. 7, the RVE consists of a rectangular prismatic FE Unit Cell (FE-UC) of volume $V = a_1 \times a_2 \times \sqrt{3}a_2$, with one fiber at the center and a quarter of a fiber at each corner. The microstructure of composite is assumed to be periodically arranged and, therefore, periodic boundary conditions are implemented using coupling constraint equations (for further details see e.g. [48]). In this manner, once a deformation state is applied, each UC in the composite has the same deformation mode and there is no separation nor overlap between neighboring UCs. Given the fact that the equivalent fibers are transversely isotropic, the analysis of such UCs also yields transversely isotropic stiffness tensors. Therefore, the stress- strain relation can be represented in Voigt notation as:

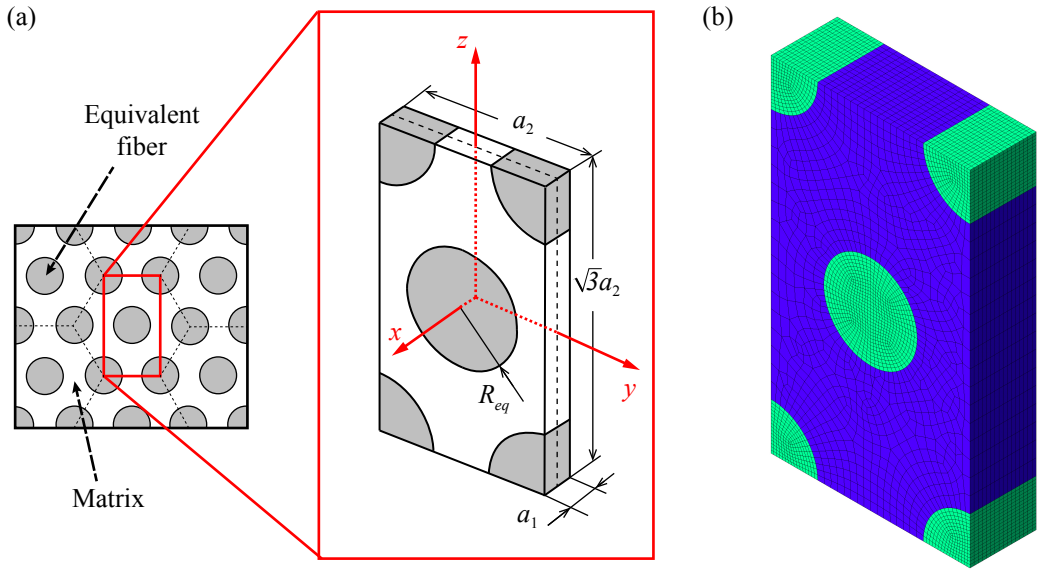

Figure 7: Periodic UC for hexagonal packing unidirectional fiber composites (a) and 3D view of FE mesh (b).

$$\begin{Bmatrix} \overline{\sigma}_1 \\ \overline{\sigma}_2 \\ \overline{\sigma}_3 \\ \overline{\sigma}_4 \\ \overline{\sigma}_5 \\ \overline{\sigma}_6 \end{Bmatrix} = \begin{bmatrix} C_{11} & C_{12} & C_{12} & 0 & 0 & 0 \\ C_{12} & C_{22} & C_{23} & 0 & 0 & 0 \\ C_{12} & C_{23} & C_{22} & 0 & 0 & 0 \\ 0 & 0 & 0 & \frac{1}{2}(C_{22} - C_{23}) & 0 & 0 \\ 0 & 0 & 0 & 0 & C_{66} & 0 \\ 0 & 0 & 0 & 0 & 0 & C_{66} \end{bmatrix} \begin{Bmatrix} \overline{\varepsilon}_1 \\ \overline{\varepsilon}_2 \\ \overline{\varepsilon}_3 \\ \overline{\varepsilon}_4 \\ \overline{\varepsilon}_5 \\ \overline{\varepsilon}_6 \end{Bmatrix} \tag{22}$$

where over bars indicate average over the volume of the RVE. When a certain strain field, $\varepsilon_{ij}^{\mathrm{o}}$, is applied to the periodic RVE, it is possible to calculate the average stress $\overline{\sigma}_{ij}$ and strain fields $\overline{\varepsilon}_{ij} = \varepsilon_{ij}^{\mathrm{o}}$ in the UC. Hence, through the application of six unit strain fields, $\overline{\varepsilon}_j = \varepsilon_j^{\mathrm{o}}$ in Voigt form, the macroscopic elastic matrix of the composite can be computed, one column at a time, as:

$$C_{ij} = \overline{\sigma}_i = \frac{1}{V}\int_V \sigma_i(x,y,z)\mathrm{d}V, \quad \text{with } \overline{\varepsilon}_j = 1, \quad i,j = 1\ldots 6 \tag{23}$$

The volume fraction of the equivalent fibers, f_{eq}, can be related to the geometric dimensions of the UC in Fig. 7, as follows:

$$f_{\mathrm{eq}} = \frac{\pi}{2\sqrt{3}}\left(\frac{R_{\mathrm{eq}}}{a_2}\right)^2 \tag{24}$$

The explicit modeling of random filler arrangements would require the definition of new RVEs with extremely fine mesh densities and considerable computational costs. For this reason, the direct orientational average of the previously computed constitutive tensor for fully aligned filler arrangements is used instead as follows:

$$\langle \mathbf{C} \rangle = \frac{1}{2\pi}\int_0^{2\pi}\int_0^{\pi/2} \mathbf{C}(\theta,\psi)\sin(\theta)\mathrm{d}\theta\mathrm{d}\psi \tag{25}$$

with $\mathbf{C}(\theta,\psi)$ being the stiffness tensor in Eq. (22) defined in a rotated coordinate system with Euler angles, θ and ψ. Let us note that a similar approach was proposed by Schjødt-Thomsen and Pyrz [49] as an alternative to the conventional MT method.

3. Results and discussion

The numerical results are organized into three parts. First, the estimates of the elastic moduli of isolated SWCNTs and MWCNTs are validated with results retrieved from the literature. Afterwards, the efficiency parameters are fitted by polynomial expressions using the micromechanics approaches presented in Section 2.2 on the basis of the developed representative equivalent fibers. Finally, parametric analyses are performed to investigate the sensitivity of the macroscopic response of CNT-reinforced polymer composites.

3.1. Validation of the CNT simulations

The developed approach is benchmarked against previously published results from the literature. The goal is not only to prove that the results are reliable and that fall within acceptable ranges, but also to seek and identify possible limitations of the numerical model. In particular, the estimates on Young's moduli of SWCNTs and MWCNTs are used for comparison.

3.1.1. Isolated SWCNTs

All the benchmark results used for validation were obtained from numerical simulations, except those reported by Shen and Li [10] who derived closed-form solutions for the Young's modulus of SWCNTs. Tables 1 and 2 present the results for armchair (n,n) and zig-zag $(n,0)$ SWCNTs, respectively.

Table 1: Comparison of Young's moduli, E, for different isolated armchair SWCNTs.

Reference	Method	Chirality	E [TPa]
[10]	Analytic	(5,5)	1.2121
[50]	FEM	(5,5)	0.9200
[51]	FEM	(5,5)	0.9400
Present	FEM	(5,5)	1.0700
[10]	Analytic	(10,10)	1.2291
[12]	FEM	(10,10)	0.9200
[52]	FEM	(10,10)	0.8810
[51]	FEM	(10,10)	0.9430
Present	FEM	(10,10)	1.0710
[53]	MD	(12,12)	0.9000
[10]	Analytic	(12,12)	1.2309
[51]	FEM	(12,12)	0.9430
Present	FEM	(12,12)	1.0710

Overall, it is observed that the present results are found in close agreement with other results from the literature. Nonetheless, it is noted that slight differences arise among the different approaches. Different factors can give an explanation for these discrepancies, namely:

Table 2: Comparison of the Young's moduli, E,for different isolated zig-zag SWCNTs.

Reference	Method	Chirality	E [TPa]
[10]	Analytic	(9,0)	1.1932
[12]	FEM	(9,0)	0.9120
[51]	FEM	(9,0)	0.9405
Present	FEM	(9,0)	1.0740
[10]	Analytic	(10,0)	1.2291
[12]	FEM	(10,0)	0.9120
[51]	FEM	(10,0)	0.9410
Present	FEM	(10,0)	1.0700
[10]	Analytic	(20,0)	1.2335
[12]	FEM	(20,0)	0.9120
[51]	FEM	(20,0)	0.9410
Present	FEM	(20,0)	1.0580

- Different type of intramolecular model are available to describe the covalent bonds. The harmonic model is used in this paper, while the Morse potential [54] was used by Meo and Rossi [50]. Harmonic models are the simplest representation and they behave reasonably well under small strain condition near the equilibrium position [55].
- Different FE software. ABAQUS was used by Doh and Lee [51].
- In the present work, it is assumed that the potential energy sum is a contribution of bond stretching, bending and torsion. Except for Rossi and Meo [12], all the other authors omitted the contribution of torsion. Apparently, the energy associated with torsion should not play an important role in the tensile behavior of a SWCNT without defects [56, 57].

In any case, the differences are rather small so the results are considered acceptable.

3.1.2. Isolated MWCNTs

A further validation of the estimates on the elastic moduli of MWCNTs implicitly means the validation of the interaction model among concentric CNTs. Several configurations of MWCNTs can be made, including different numbers of layers and chiralities. For illustrative purposes, Double-Walled CNTs (DWCNTs) are simulated and the results are compared with results retrieved from the literature. Two different types of analysis are performed. First, the same type of concentric layers (zig-zag/zig-zag or armchair/armchair) are compared with the results from Li and Chou [58], as shown in Fig. 8. Second, the results of mixed chiralities i.e. with the inner diameter being armchair and the outer diameter being zig-zag ($d_{\text{zig}} > d_{\text{arm}}$) or viceversa ($d_{\text{zig}} < d_{\text{arm}}$), are compared with the results from Doh and Lee [51] and shown in Fig. 9.

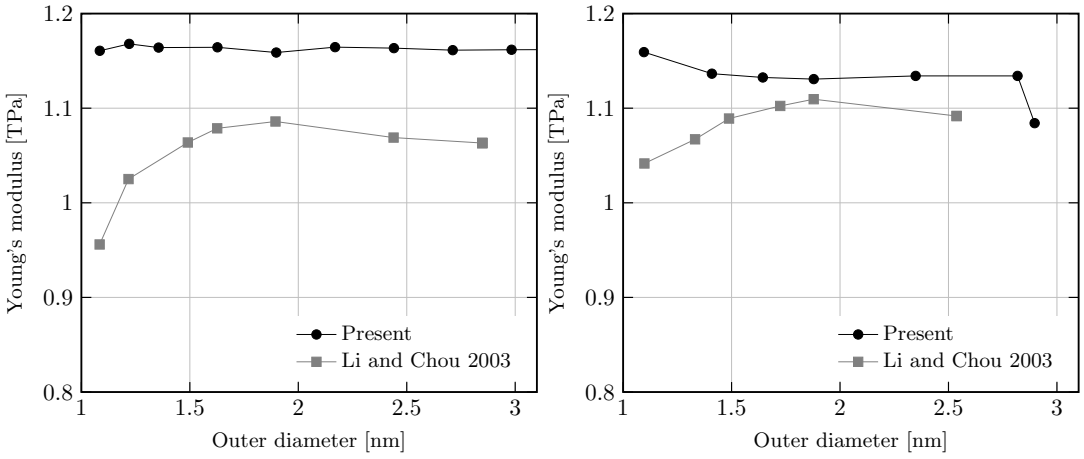

(a) Armchair-armchair.

(b) Zigzag-zigzag.

Figure 8: Comparison of the predicted Young's moduli of DWCNTs with a single configuration, for varying outer diameter.

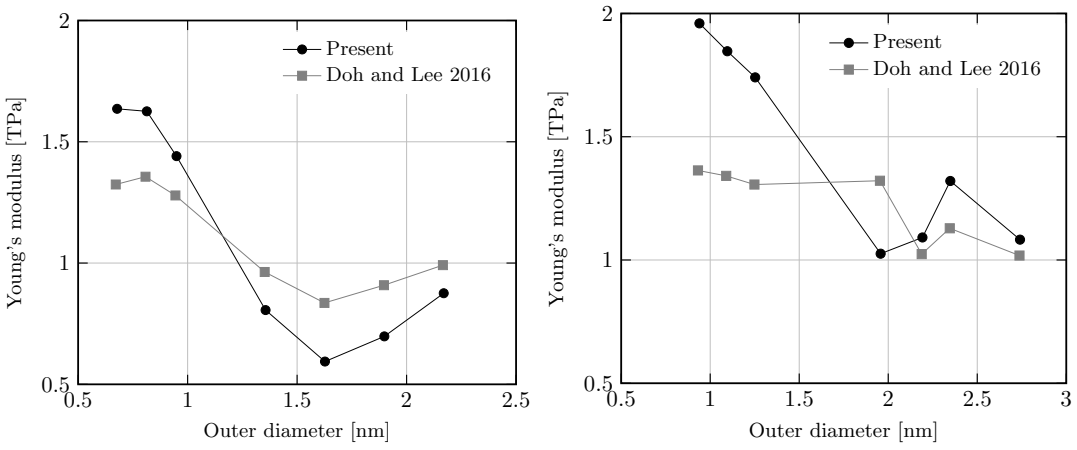

(a) $d_{\text{zig}} < d_{\text{arm}}$ (b) $d_{\text{zig}} > d_{\text{arm}}$

Figure 9: Comparison of the predicted elastic moduli of DWCNTs with two configurations, for varying outer diameter.

It is noted that the simulation results differ from the observed in the literature. In the first analysis (Fig. 8), Li and Chou [58] modeled the complete nonlinear behavior of the LJ potential, hence needing a nonlinear solution procedure. In the present simulations, the spring elements that represent the vdW interactions have a constant stiffness [40]. In this case, only a linear solution is required, greatly simplifying the analysis. Despite the observed discrepancies, the difference is rather small (< 0.1 TPa for $d_o > 1.5$ nm in both configurations).

For the second analysis (Fig. 9), the present results show higher variance than the results from Doh and Lee [51]. Those authors mentioned that the nonlinear trends observed in Fig. 9 could be due to the difference in the axial stiffness between inner SWCNT and outer SWCNT. Unfortunately, Doh and Lee [51] did not provide enough information about the modeling of the vdW forces nor the type of FE used. Nevertheless, it is remarkable that a simple linear spring model can capture this nonlinear trend, as observed in both figures.

3.2. Fitting of the EROM efficiency parameters

Two different polymers are selected as matrix phases, namely Poly (methyl methacrylate), known as PMMA, and Poly{(*m*-phenylenevinylene)-*co*-[(2,5-dioctoxy-*p*-phenylene)vinylene]}, known as PmPV. Both polymers are isotropic with Poisson's ratio $\nu^m = 0.34$ and Young's moduli E^m of 2.5 GPa for PMMA [32] and 2.1 GPa for PmPV [29]. As mentioned above, the goal of this first set of analyses is to compute the efficiency parameters as a function of the filler volume fraction, for both PmPV and PMMA matrices doped with SWCNTs and MWCNTs, assuming CNTs as infinitely long fibers.

3.2.1. Polymer doped with SWCNTs

A key aspect in the determination of the effective properties of CNT/polymer equivalent fibers is the definition of the CNT wall thickness t. As reported by Wang and Zhang [59], there exist considerable discrepancies in the literature on the definition of this critical parameter, with thickness values ranging from 0.062 to 0.69 nm. Specifically, numerous works assume a thickness value of 0.34 nm (see the references in Section 3.1.1). Nevertheless, the Vodenitcharova-Zhang criterion [60] indicates that the effective thickness of SWCNTs should be below the atomic diameter (0.142 nm). Therefore, the value of 0.34 nm is thoroughly invalid. Fig. 10 investigates the influence of t on the macroscopic longitudinal Young's modulus $E_\parallel$ of (5,5) SWCNT/PmPV composites. First, Fig. 10 (a) plots $E_\parallel$ versus the filler volume fraction f_r for different tube wall thicknesses, namely $t = 0.067$ nm, 0.1 nm, 0.142 nm, 0.2 nm and 0.34 nm. As expected, it is observed that lower thickness values lead to stiffer fillers and, consequently, to stiffer composites. Further, Fig. 10 (b) shows the relationship between t and $E_\parallel$ of PmPV loaded with $f_r = 1\%$ (5,5) SWCNTs. For illustrative purposes, the limit values of 0.34 nm and the atomic diameter 0.142 nm are remarked. It is observed that the Young's modulus is highly sensitive to t with drastic reductions caused by increasing tube wall thicknesses. In particular, a tube wall thickness of 0.34 nm approximately yields half of the Young's modulus obtained with the limit thickness of 0.142 nm indicated by the Vodenitcharova-Zhang criterion. Also, the sensitivity of $E_\parallel$ to t increases for increasing filler volume fractions as shown in Fig. 10 (a). Hence, a tube wall thickness of 0.1 nm is selected for all subsequent calculations.

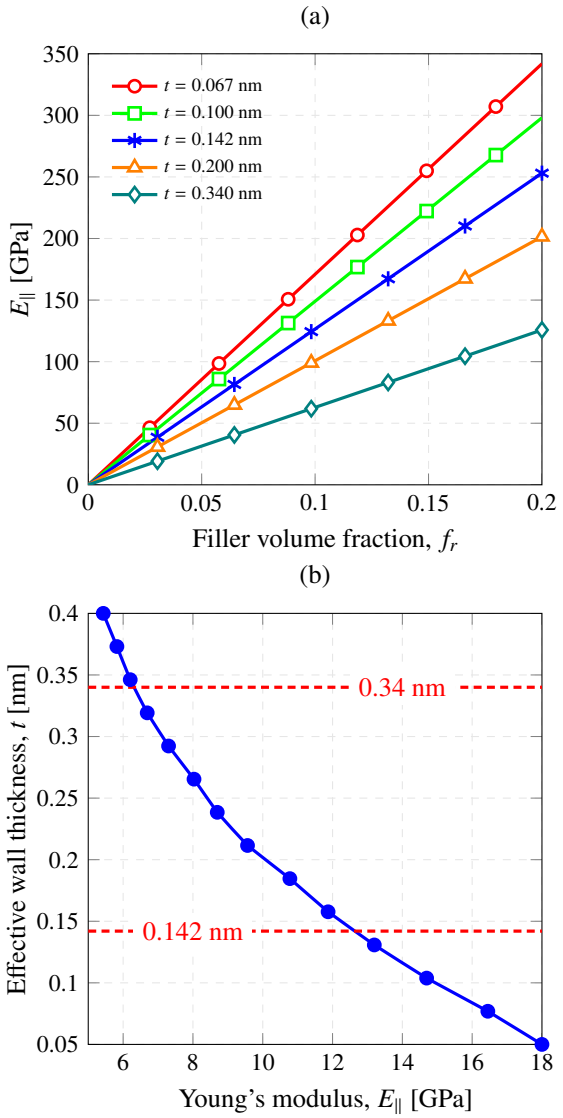

Figure 10: Longitudinal Young's modulus $E_{\|}$ of (5,5) SWCNT/PmPV versus filler volume fraction f_r for varying CNT wall thicknesses t (a), and t versus $E_{\|}$ of (5,5) SWCNT/PmPV with a filler volume fraction $f_r = 1\%$.

Once the tube wall thickness is fixed to $t = 0.1$ nm, the elastic moduli of different isolated zig-zag and armchair SWCNTs are computed and their resulting five Hill's elastic moduli are shown in Table 3. In addition, Table 4 collects the effective Hill's moduli of the effective fibers for SWCNT/PmPV and SWCNT/PMMA composites, computed as described in Section 2.1.3. Hence, the microscopic elastic properties of the composites can be scaled up by means of the MT model and the numerical FE-UC. Fig. 11 shows the Young's moduli (the longitudinal $E_{\|}$ and the transverse $E_{\perp}$) and the shear modulus G_{12} of (10,10) SWCNT/PmPV composites versus the filler volume fraction. It is important to note that, in practice, CNT concentrations dot not usually exceed 5-10% [4]. The reason lies in the fact that obtaining uniform filler dispersions at high concentrations is an intricate task due to the tendency of CNTs to agglomerate in bundles. Owing to the high specific surface of CNTs, large vdW interactions take place among nanotubes, favoring the appearance of filler agglomerates [61]. It has been extensively reported in the literature that agglomerates behave as defects in the microstructure, leading to substantial decreases in the stiffening efficiency of CNTs [61–63]. For illustrative purposes, a wider range of variation of the CNT volume fraction from 0 to 0.2 has been defined in these analyses. Nevertheless, it must be kept in mind that estimates for filler volume fractions above 0.1 may become uncertain and the effects of agglomeration should be incorporated. In Fig. 11, the estimates provided by the ROM ($\eta_1 = \eta_2 = \eta_3 = 1$) and the filler properties from Table 3 are also included with blue dashed lines. It is noted that very close agreements are found between MT and FE-UC solutions, with small differences in the shear modulus G_{12} at high filler contents. This similarity is expected since the MT model considers far-field interaction between inclusions, an assumption that is especially well-suited for low filler contents, as it is the case for CNT-reinforced composites. Conversely, large differences are found for the

ROM estimates since no explicit particle interaction is considered.

Table 3: Hill's elastic moduli of (n, m) SWCNTs ($t = 0.10$ nm).

n	m	k_r [GPa]	l_r [GPa]	$m_r = p_r$ [GPa]	n_r [GPa]
5	5	1212.28	896.21	1285.15	4282.01
9	9	676.00	496.12	1304.26	3998.59
10	10	608.59	446.39	1305.93	3963.30
12	12	507.36	371.87	1308.12	3910.38
15	15	406.03	297.44	1309.91	3857.53
20	20	304.60	223.07	1311.32	3804.84
5	0	2103.26	1966.41	1647.97	6284.23
9	0	1186.03	925.32	1442.01	4528.06
10	0	1068.36	820.88	1428.58	4391.91
12	0	891.25	671.31	1411.85	4210.24
15	0	713.57	528.83	1398.77	4051.90
20	0	535.49	391.92	1388.97	3913.36

Table 4: Hill's elastic moduli of (n, m) SWCNT-reinforced PmPV and PMMA composites ($t = 0.10$ nm).

SWCNT		PmPV				PMMA				k_f
n	m	k_r [GPa]	l_r [GPa]	$m_r = p_r$ [GPa]	n_r [GPa]	k_r [GPa]	l_r [GPa]	$m_r = p_r$ [GPa]	n_r [GPa]	
5	5	5.475	3.780	11.929	294.784	6.517	4.499	12.016	295.642	2.791
9	9	6.140	4.429	31.964	291.222	7.307	5.271	32.069	292.162	2.458
10	10	6.318	4.520	37.291	286.139	7.519	5.379	37.401	287.079	2.392
12	12	6.683	4.882	47.596	274.890	7.951	5.808	47.714	275.878	2.277
15	15	7.246	5.438	63.842	261.103	8.618	6.465	63.970	262.164	2.136
20	20	8.204	6.226	86.879	237.715	9.751	7.400	87.021	238.868	1.957
5	0	5.119	3.319	3.204	358.065	6.094	3.952	3.279	358.857	3.091
9	0	5.469	3.613	14.183	360.167	6.510	4.300	14.275	360.986	2.796
10	0	5.562	3.708	18.158	362.358	6.621	4.413	18.253	363.187	2.737
12	0	5.755	3.887	24.028	344.642	6.850	4.627	24.130	345.492	2.629
15	0	6.056	3.973	34.025	326.742	7.208	4.730	34.135	327.576	2.492
20	0	6.580	4.633	49.155	297.620	7.829	5.512	49.276	298.556	2.308

Then, it is possible to estimate the efficiency parameters of the EROM by means of Eqs. (20) in order to fit the MT or the FE-UC estimates, which do take into consideration the CNT-polymer interactions. Fig. 12 shows the resulting efficiency parameters on the basis of the MT results previously reported in Fig. 11. It is observed that the efficiency parameter η_1 remains approximately constant and below one. On the contrary, η_2 and η_3 are constantly above one and increasing with the filler volume fraction. At this point, different regression models were contemplated in order to provide analytical expressions for the efficiency parameters. However, it was found that the consideration of a constant value for η_1, along with linear regression models for η_2 and η_3 (shown in Fig. 12), provides very close fittings with coefficients of determination above 95%. Therefore, the efficiency parameters can be defined as functions of the filler volume fraction f_r as follows:

$$\eta_1(f_r) = a_{0,1}, \quad f_r \in [0.01, 0.2] \tag{26a}$$

$$\eta_2(f_r) = a_{0,2} + a_{1,2} f_r, \quad f_r \in [0.01, 0.2] \tag{26b}$$

$$\eta_3(f_r) = a_{0,3} + a_{1,3} f_r, \quad f_r \in [0.01, 0.2] \tag{26c}$$

In this way, the best-fitting parameters $a_{i,j}$ in Eq. (26) are obtained for all the considered SWCNT-reinforced PmPV and PMMA composites and are presented in Table 5.

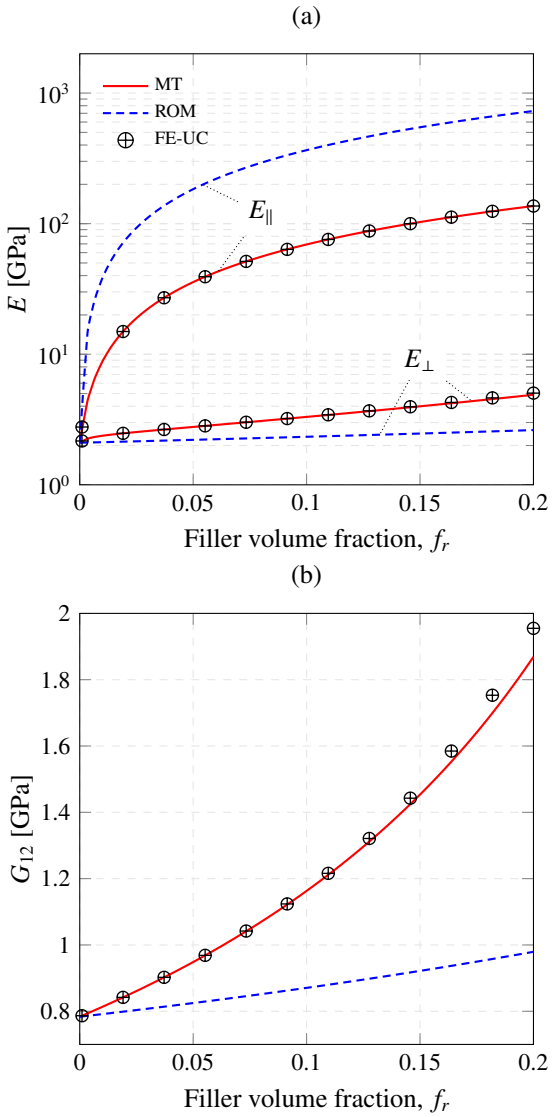

Figure 11: Young's moduli E (a) and shear modulus G_{12} (b) versus filler volume fraction f_r for fully aligned (10,10) SWCNT-reinforced PmPV.

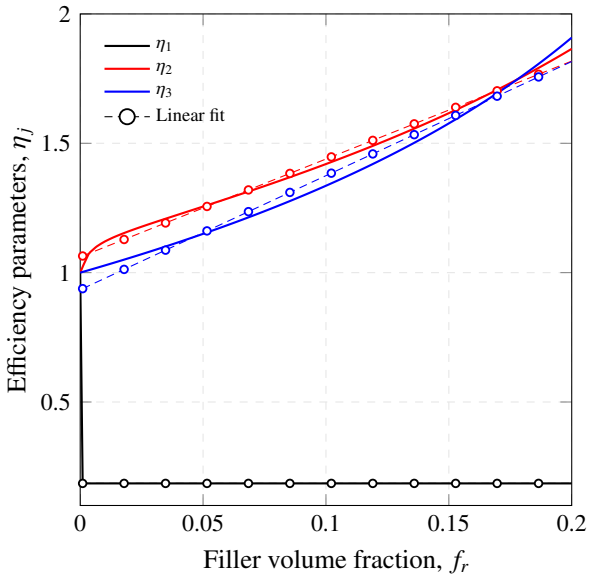

Figure 12: Efficiency parameters η_j ($j = 1, 2, 3$) versus filler volume fraction for (10,10) SWCNT-reinforced PmPV ($t =$ 0.1 nm).

Table 5: Best-fitting parameters for the linear regression of the efficiency parameters η_j ($j = 1, 2, 3$) for SWCNT/PmPV and SWCNT/PMMA composites (($t = 0.1$ nm, $f_r \in [0.01, 0.2]$).

		PmPV					PMMA				
n	m	η_1	η_2		η_3		η_2	η_1		η_3	
		$a_{0,1}$	$a_{0,2}$	$a_{1,2}$	$a_{0,3}$	$a_{1,3}$	$a_{0,1}$	$a_{0,2}$	$a_{1,2}$	$a_{0,3}$	$a_{1,3}$
5	5	0.224	1.049	4.391	0.912	5.263	0.224	1.049	4.257	0.918	5.035
9	9	0.194	1.057	3.940	0.930	4.612	0.194	1.055	3.902	0.932	4.538
10	10	0.185	1.059	3.799	0.935	4.403	0.185	1.057	3.770	0.936	4.342
12	12	0.169	1.062	3.538	0.944	4.021	0.169	1.060	3.521	0.945	3.979
15	15	0.150	1.066	3.215	0.955	3.557	0.150	1.063	3.208	0.955	3.529
20	20	0.125	1.070	2.811	0.967	2.992	0.125	1.067	2.812	0.967	2.975
5	0	0.246	1.078	3.122	0.960	3.338	0.247	1.082	2.772	0.970	2.848
9	0	0.262	1.049	4.525	0.906	5.492	0.262	1.049	4.408	0.912	5.289
10	0	0.261	1.049	4.505	0.906	5.472	0.261	1.049	4.416	0.911	5.314
12	0	0.242	1.052	4.324	0.914	5.199	0.242	1.051	4.263	0.917	5.086
15	0	0.220	1.056	4.046	0.925	4.777	0.220	1.055	4.009	0.927	4.705
20	0	0.187	1.062	3.619	0.941	4.145	0.187	1.060	3.602	0.942	4.102

Figures 13 (a) and (b) show the Young's moduli of fully aligned and randomly oriented (10,10) SWCNT-reinforced PmPV and PMMA composites, respectively. The estimates of the present multi-scale approach are depicted for both the FE-UC and MT micromechanics approaches. It is first observed that composites doped with fully aligned fillers exhibit high degrees of anisotropy, while randomly oriented filler arrangements lead to elastically isotropic composites. Also, less stiff composites are obtained in the latter case, with the overall Young's modulus comprised between the longitudinal and transverse elastic moduli of the fully aligned counterpart. With regard to the different micromechanics approaches, very similar results are found in the case of fully aligned filler configurations. In the case of randomly oriented filler arrangements, the estimates of the MT and the FE-UC approaches have been computed by Eqs. (15) and (25), respectively, considering a constant ODF of value $\Omega(\theta, \psi) = 1/2\pi$. It is noted that the latter approach yields slightly lower estimates than the MT approach at high filler contents. These discrepancies have the same explanation as those discussed by Schjødt-Thomsen and Pyrz [49]. Those authors demonstrated that the direct orientational average of the MT results provides less stiff estimates than the conventional MT model for composites loaded with randomly oriented fillers. Furthermore, the proposed approach by Schjødt-Thomsen and Pyrz was shown to be superior for composites doped with high filler volume fractions, providing estimates comprised within the Hashin-Shtrikman-Walpole bounds for randomly oriented filler arrangements, unlike the conventional MT model.

Finally, the estimates of the EROM are plotted considering the efficiency parameters defined in Eq. (26) and the fitting parameters $a_{i,j}$ from Table 5. Very close agreements with both the MT and FE-UC approaches are found

for fully aligned filler arrangements. Although larger discrepancies are found at high filler contents when CNTs are randomly oriented (Eq. (21)), the largest differences are below 30 GPa. It is concluded that the accuracy of the proposed simplified approach is sufficiently acceptable.

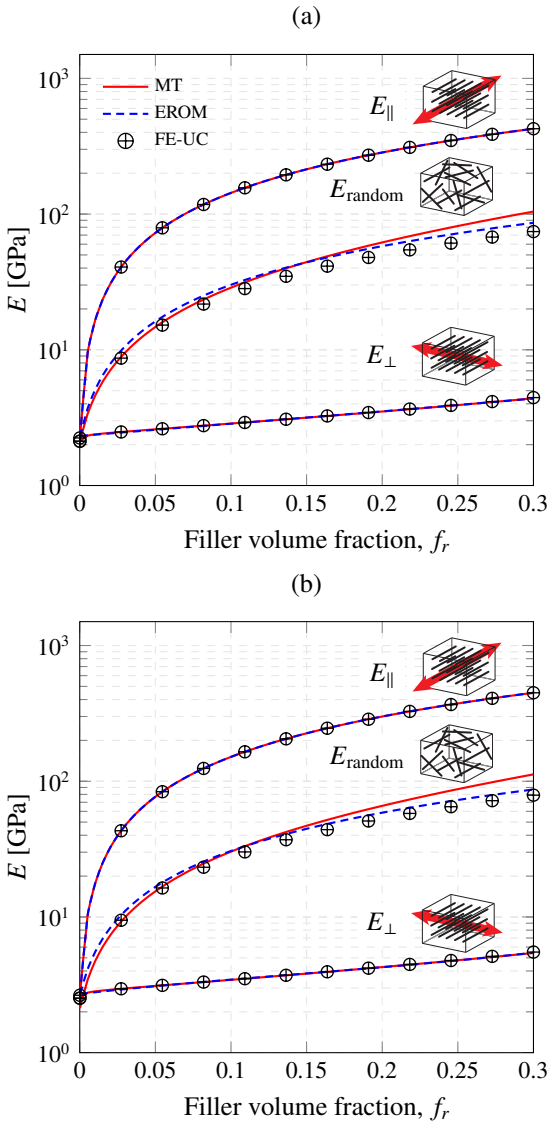

Figure 13: Young's moduli E of (10,10) SWCNT-reinforced PmPV (a) and PMMA (b) composites versus filler volume fraction f_r for fully aligned and randomly oriented configurations ($t = 0.1$ nm).

3.2.2. Polymer doped with MWCNTs

In a similar way to the previous analyses, the macroscopic behavior of composites doped with MWCNTs is investigated in this section. In particular, twelve DWCNTs (armchair/armchair and zig-zag/zig-zag), as well as two Four-Walled CNTs (FWCNTs) are studied. With regard to the tube wall thickness, in this set of analyses a value of $t = 0.1$ nm is also assumed. Firstly, the elastic moduli of the isolated MWCNTs are computed by the present atomistic-based continuum modeling and collected in Table 6. For notational convenience, the studied CNTs are denoted with an identification number (Id.) from 1 to 14. Afterwards, the elastic moduli of the corresponding equivalent fibers are computed and shown in Table 7. Figures. 14 (a) and (b) show the Young's moduli, $E_{\parallel}$ and $E_{\perp}$, and the shear modulus G_{12}, respectively, of (7,7)-(14,14) MWCNT/PmPV composites versus the filler volume fraction. It is interesting to note that, in this case, the estimates of the ROM and the MT and FE-UC approaches are closer than in the previous case study of Fig. 4. Conversely, larger discrepancies are found for the macroscopic shear modulus G_{12}. It is also observed that, in this particular case, the studied MWCNT exhibit a lesser degree of anisotropy.

Table 6: Hill's elastic moduli of MWCNTs ($t = 0.10$ nm).

Chilarity	Id.	k_r [GPa]	l_r [GPa]	$m_r = p_r$ [GPa]	n_r [GPa]
(5,5)-(10,10)	1	1984.203	900.530	732.703	2210.538
(6,6)-(12,12)	2	2443.688	1195.038	593.757	2040.452
(7,7)-(14,14)	3	2443.688	899.951	524.279	1598.251
(8,8)-(16,16)	4	2443.688	898.447	471.743	1463.653
(9,9)-(18,18)	5	2443.688	897.436	428.663	1354.868
(10,10)-(20,20)	6	2443.688	896.730	392.725	1265.117
(5,0)-(10,0)	7	9200.112	1777.782	1486.743	3969.229
(6,0)-(12,0)	8	6920.968	1491.827	1324.120	3329.875
(7,0)-(14,0)	9	3471.225	1134.352	1032.984	2825.563
(8,0)-(16,0)	10	2500.854	942.275	837.074	2414.911
(9,0)-(18,0)	11	2565.389	1082.967	727.181	2187.179
(10,0)-(20,0)	12	3262.808	1295.913	653.616	2055.039
(5,5)-(10,10)-(15,15)-(20,20)	13	3258.650	860.642	591.929	1700.097
(5,0)-(10,0)-(15,0)-(20,0)	14	23637.980	1726.684	1709.083	3544.465

Table 7: Hill's elastic moduli of MWCNT/PmPV and MWCNT/PMMA composites ($t = 0.10$ nm).

Id.	PmPV				PMMA				k_f
	k_r [GPa]	l_r [GPa]	$m_r = p_r$ [GPa]	n_r [GPa]	k_r [GPa]	l_r [GPa]	$m_r = p_r$ [GPa]	n_r [GPa]	
1	6.320	4.475	41.256	385.529	7.521	5.325	41.366	386.456	2.392
2	6.684	5.212	50.443	359.593	7.953	6.200	50.560	360.673	2.277
3	6.684	4.890	58.760	346.227	7.953	5.818	58.886	347.204	2.179
4	6.684	4.890	70.050	346.227	7.953	5.911	70.183	337.835	2.179
5	6.684	5.075	78.209	325.601	7.953	6.038	78.349	326.606	2.021
6	6.684	5.073	88.931	317.470	7.953	6.036	89.076	318.463	1.957
7	5.563	3.743	22.231	526.263	6.622	4.455	22.326	527.101	2.737
8	5.755	3.961	29.820	497.565	6.851	4.715	29.920	498.434	2.629
9	5.955	4.098	35.776	469.717	7.088	4.878	35.882	470.595	2.535
10	6.160	4.322	39.825	438.951	7.331	5.144	39.936	439.860	2.451
11	6.369	4.582	46.188	409.900	7.580	5.453	46.305	410.851	2.376
12	6.582	4.549	52.168	392.686	7.832	5.413	52.289	393.600	2.308
13	8.230	5.955	124.004	536.733	9.787	7.082	124.145	537.811	1.957
14	6.584	4.754	93.891	800.605	7.835	5.658	94.011	801.574	2.308

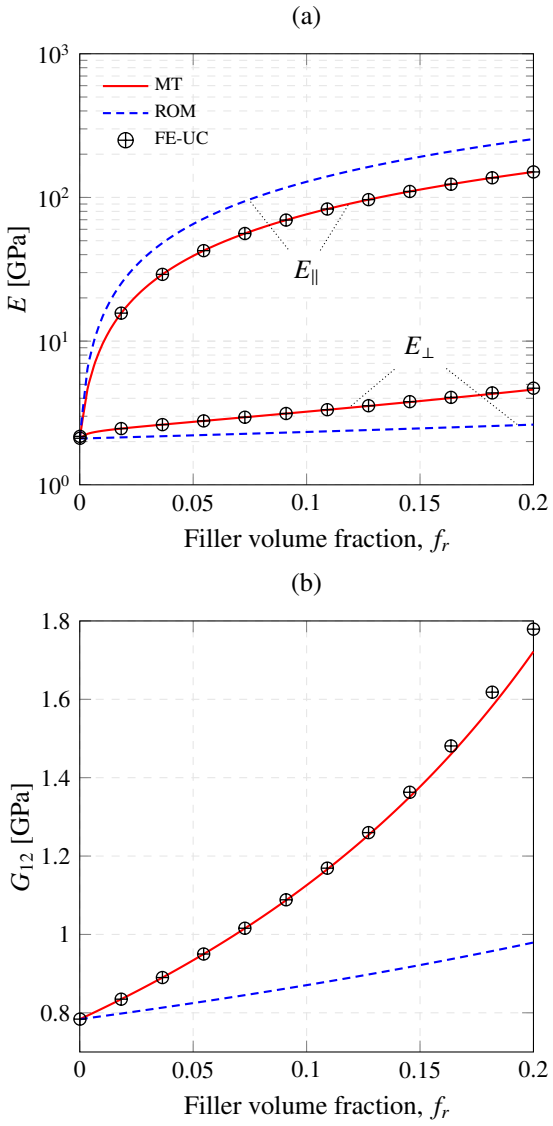

Figure 14: Young's moduli E (a) and shear modulus G_{12} (b) versus filler volume fraction f_r for fully aligned (7,7)-(14,14) MWCNT-reinforced PmPV ($t = 0.10$ nm).

With regard to the fitting of the efficiency parameters, the procedure is identical to the previous set of analyses. Linear regression models for the definition of η_j ($j = 1, 2, 3$) as functions of the CNT content were found suitable for filler volume fractions ranging from 0 to 0.2, with determination coefficients above 95%. Table 8 collects the best-fitting parameters $a_{i,j}$ for all the studied MWCNT-reinforced composites. It is worth noting that the efficiency parameters η_1, which modulate the stiffening capability of CNTs along the longitudinal direction in Eq. (20a), exhibit considerably higher values than those for SWCNTs. This fact gives an explanation to the lesser differences between the ROM and the MT and FE-UC approaches. The study of the efficiency parameters is particularly interesting because it gives some insight into the load transfer capability of the CNT/polymer interphases. For instance, values of η_1 close to 1 indicates the presence of interphases with elastic properties similar to the matrix material. On the other hand, small values of η_1 evidence the existence of soft interphases.

Table 8: Best-fitting parameters for the linear regression of the efficiency parameters η_j ($i = 1, 2, 3$) for MWCNT/PmPV and MWCNT/PMMA composites ($t = 0.1$ nm, $f_r \in [0.01, 0.2]$).

Id.	PmPV					PMMA				
	η_1	η_2		η_3		η_2	η_1		η_3	
	$a_{0,1}$	$a_{0,2}$	$a_{1,2}$	$a_{0,3}$	$a_{1,3}$	$a_{0,1}$	$a_{0,2}$	$a_{1,2}$	$a_{0,3}$	$a_{1,3}$
1	0.506	1.063	3.801	0.934	4.435	0.506	1.061	3.775	0.936	4.380
2	0.554	1.067	3.528	0.944	4.036	0.554	1.064	3.511	0.945	3.996
3	0.587	1.071	3.257	0.952	3.702	0.588	1.068	3.247	0.952	3.671
4	0.657	1.071	3.276	0.951	3.730	0.614	1.071	3.028	0.958	3.406
5	0.632	1.076	2.839	0.963	3.194	0.632	1.073	2.838	0.963	3.174
6	0.654	1.078	2.676	0.967	2.996	0.654	1.075	2.677	0.967	2.980
7	0.394	1.051	4.586	0.902	5.635	0.394	1.051	4.510	0.906	5.500
8	0.431	1.055	4.380	0.911	5.321	0.431	1.054	4.329	0.913	5.227
9	0.481	1.059	4.159	0.920	4.983	0.481	1.058	4.121	0.922	4.910
10	0.517	1.062	3.948	0.928	4.663	0.517	1.060	3.918	0.930	4.603
11	0.557	1.064	3.772	0.935	4.399	0.557	1.062	3.750	0.936	4.350
12	0.582	1.067	3.611	0.941	4.160	0.582	1.065	3.594	0.942	4.119
13	0.706	1.084	2.775	0.966	3.021	0.706	1.081	2.777	0.966	3.009
14	0.537	1.074	3.638	0.939	4.256	0.537	1.072	3.630	0.939	4.233

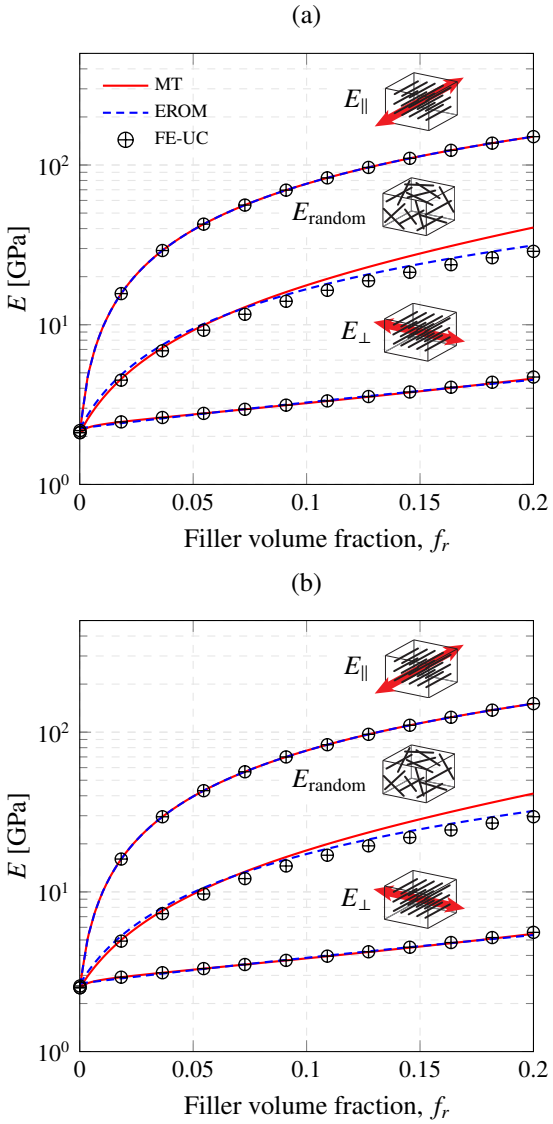

Figure 15: Young's moduli of (7,7)-(14,14) MWCNT-reinforced PmPV (a) and PMMA (b) composites versus filler volume fraction f_r for fully aligned and randomly oriented configurations ($t = 0.10$ nm).

Finally, the Young's moduli of fully aligned and randomly oriented (7,7)-(14,14) MWCNT-reinforced PmPV and PMMA composites are shown in Fig. 15 (a) and (b), respectively. In this case, close results are also found between the different approaches and, therefore, the proposed simplified EROM is considered acceptable for the modeling of MWCNT-reinforced composites.

3.3. Sensitivity analyses

In this last section, numerical results are presented to investigate the sensitivity of the macroscopic elastic properties of CNT-reinforced polymer composites on the CNT chirality, volume fraction and aspect ratio. Fig. 16 plots the longitudinal elastic moduli versus the filler volume fraction for infinitely long SWCNT-reinforced PmPV composites. Both armchair and zig-zag CNT structures are studied, as well as fully aligned and randomly oriented filler arrangements. In this case, only the multiscale approach consisting of the atomistic-based continuum modeling and the MT approach are used. The elastic properties of the equivalent fibers are taken from Table 4. In the case of fully aligned configurations, the longitudinal $E_{\parallel}$ and transverse $E_{\perp}$ elastic moduli are represented with solid and dashed lines, respectively. In a similar way to previously reported results in the literature (e.g. [64]), it is observed that zig-zag CNTs exhibit stiffer responses than the armchair ones, especially for small tube diameters. In order to strengthen this analysis, Fig. 17 shows the longitudinal $E_{\parallel}$ as a function of the CNT diameter for composites with a filler volume fraction of $f_r = 0.05$. For illustrative purposes, the results for (10,10) and (10,0) SWCNTs are remarked. Three observations can be made. First, the Young's modulus monotonically decreases with the increase of CNT diameter and for every CNT configuration. Second, for every tube diameter the zig-zag CNTs yield slightly higher Young's moduli. Third, the differences between the two curves become smaller with increasing diameters.

Fig. 18 shows the variation of $E_{\parallel}$ with the increase of the CNT aspect ratio for the previously considered SWCNTs. Within the Mori-Tanaka framework, the geometry of the inclusions is taken into consideration in the definition of the Eshelby's tensor $\mathbf{S}$. Let us recall that the main assumption in the Eshelby's theory is that inhomogeneities can be defined as ellipsoids. Hence, the aspect ratio of the CNTs can be taken into consideration by equating the CNT length and diameter to the semi-major and semi-minor axes of the ellipsoids, respectively. For further information about the specific definition of the Eshelby's tensor $\mathbf{S}$, readers are invited to consult the reference [45]. Let us simply indicate that, in the case of isotropic materials doped with transversely isotropic ellipsoidal inclusions, $\mathbf{S}$ depends on the geometry of the inclusions and the Poisson's ratio of the matrix. It is observed in Fig. 18 that $E_{\parallel}$ dramatically increases with increasing CNT aspect ratios. It can be also seen that further increases in the CNT aspect ratio beyond 10^3 result in relatively small increases in the effective longitudinal Young's modulus. This is typically the case for CNT-reinforced composites and, therefore, these results justify the common assumption of CNTs as infinitely long fillers. It is also interesting to note that, in the case of zig-zag CNTs, the influence of the CNT aspect ratio on the overall elastic modulus is higher than in the case of armchair CNTs, especially for CNTs with small tube diameters.

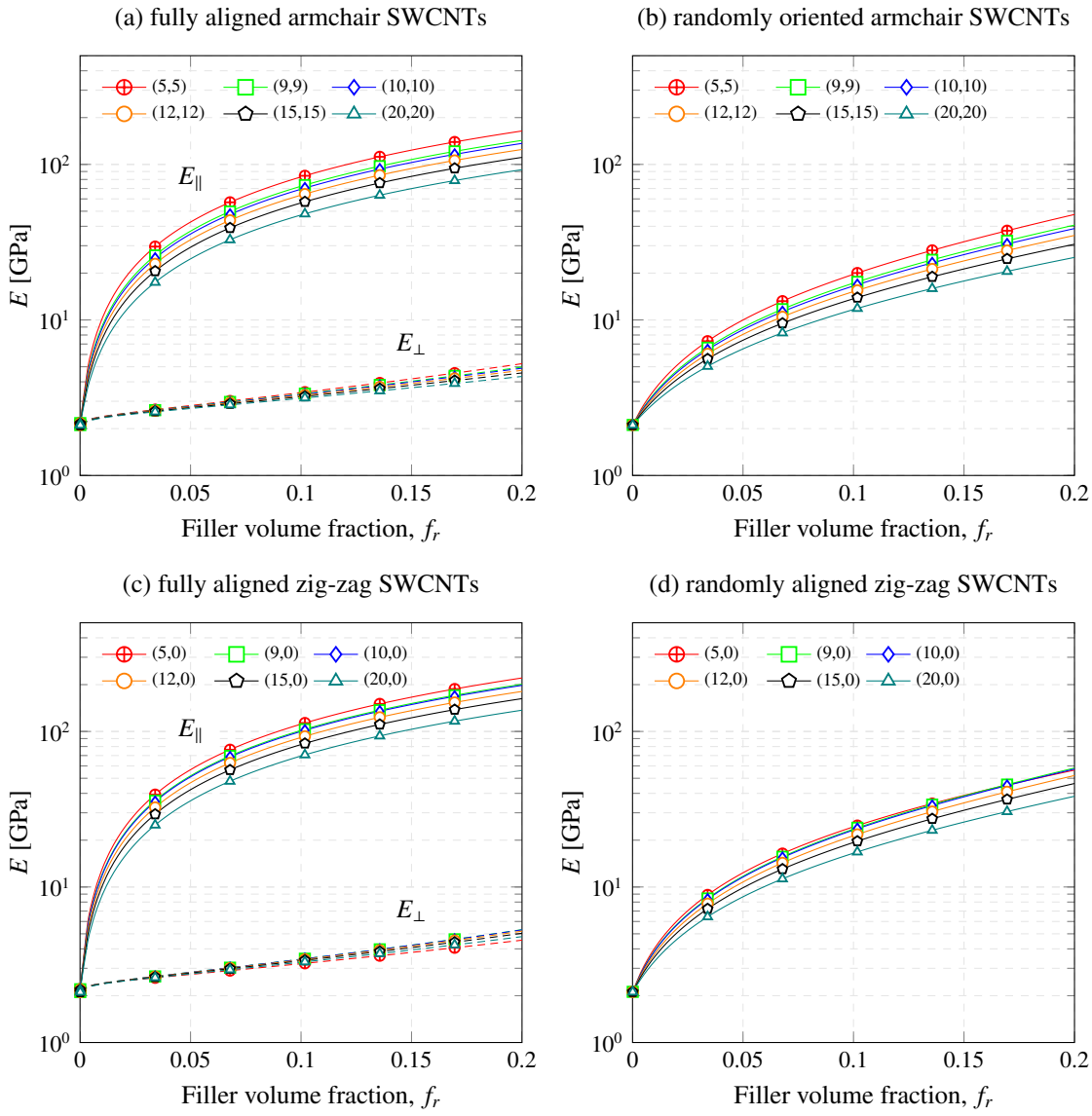

Figure 16: Variation of the elastic moduli with the CNT volume fraction for SWCNT-reinforced PmPV for armchair (n,n) (a,b) and zig-zag $(n,0)$ (c,d) CNT types ($t = 0.10$ nm).

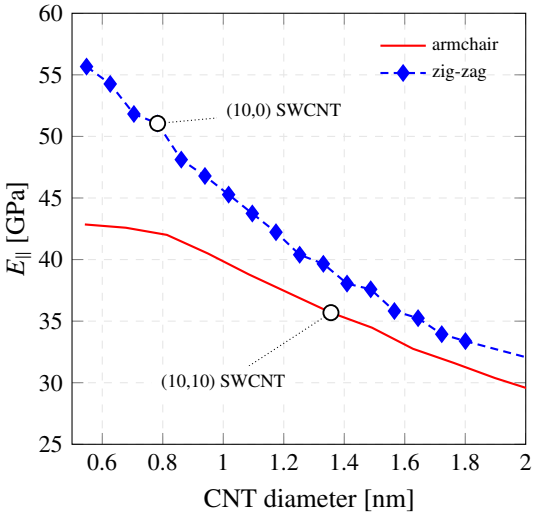

Figure 17: Variation of the longitudinal Young's modulus $E_{\|}$ with the CNT diameter for SWCNT-reinforced PmPV for armchair (n,n) and zig-zag $(n,0)$ CNT types ($t = 0.10$ nm, $f_r = 5\%$).

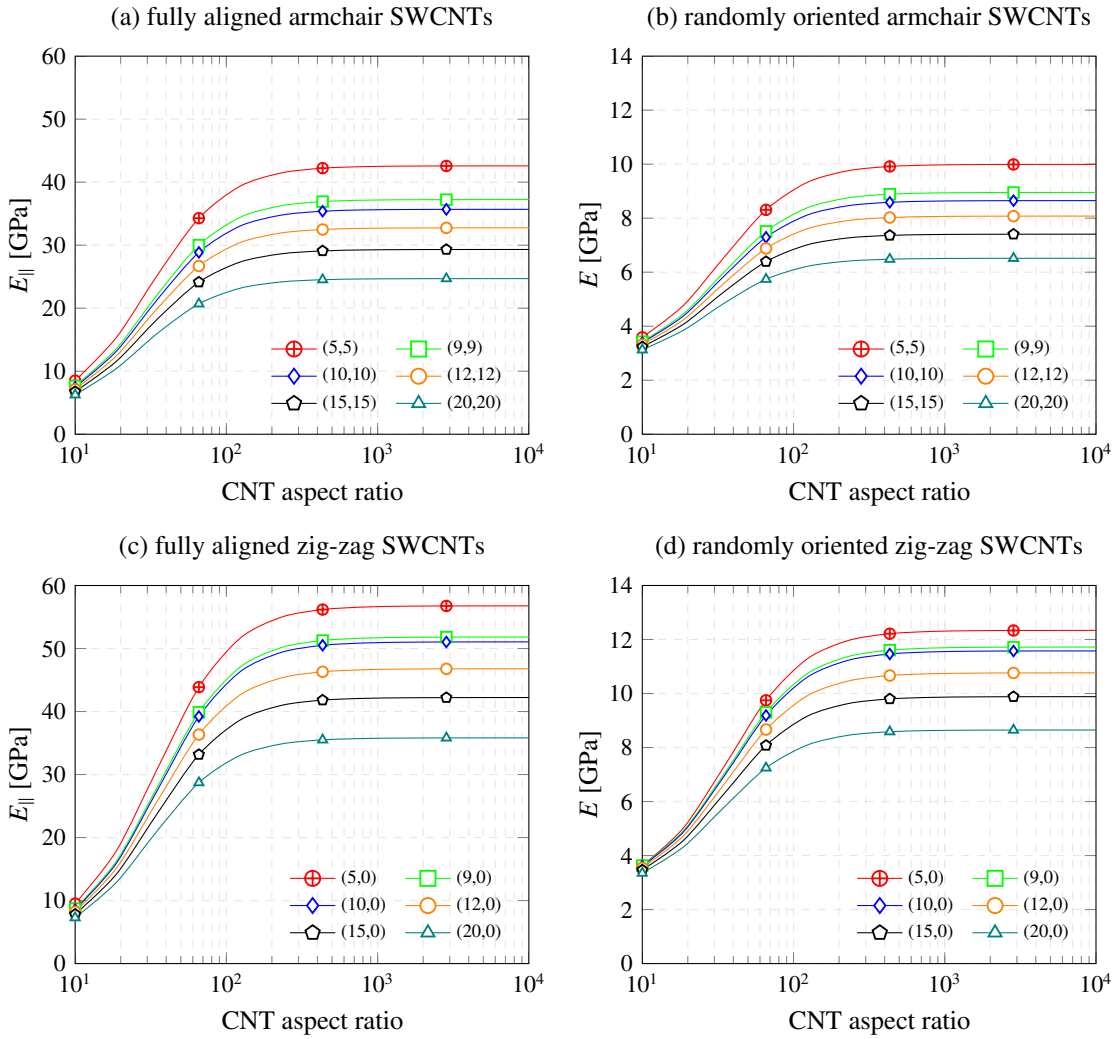

Figure 18: Variation of $E_{\|}$ with the CNT aspect ratio for SWCNT-reinforced PmPV for armchair (n,n) (a,b) and zig-zag $(n,0)$ (c,d) CNT types ($t = 0.10$ nm, $f_r = 5\%$).

With regard to MWCNT-reinforced composites, Fig. 19 (a) and (b) plot the longitudinal elastic moduli versus

filler volume fraction for infinitely long MWCNT-reinforced PmPV with fully aligned and randomly oriented filler configurations, respectively. Identification numbers 1 to 14 correspond to the chiralities previously shown in Table 6. It is observed that (5,0)-(10,0)-(15,0)-(20,0) MWCNTs (Id. 14) yield the highest Young's moduli, whilst (10,10)-(20,20) MWCNTs (Id. 6) yield the lowest values. Finally, Fig. 20 furnishes the relationship between the elastic moduli of MWCT/PmPV composites and the CNT aspect ratio.

(a) fully aligned MWCNTs

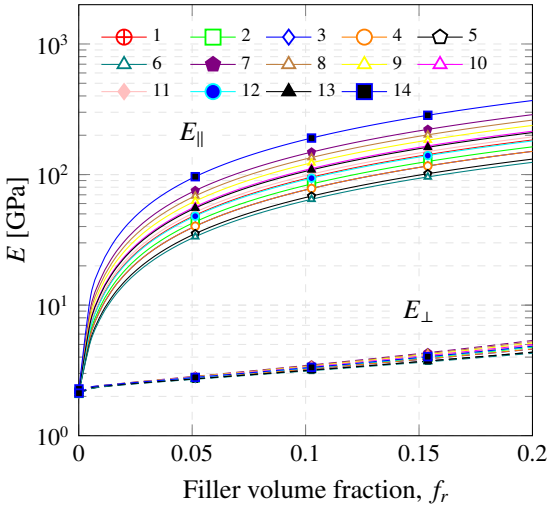

(b) randomly oriented MWCNTs

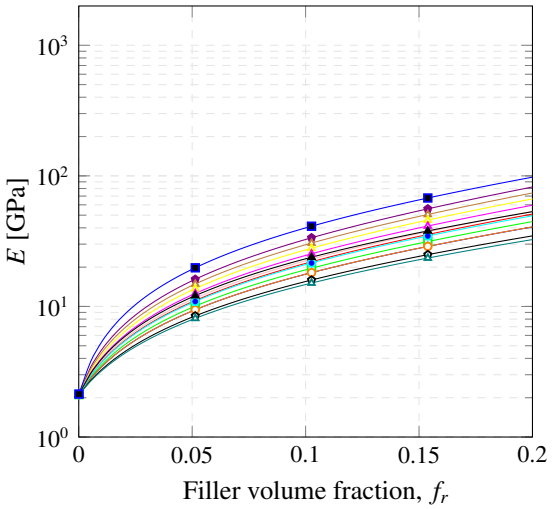

Figure 19: Variation of the elastic moduli with the CNT volume fraction for PmPV doped with fully aligned MWCNTs (a) and randomly oriented MWCNTs (b) ($t = 0.10$ nm).

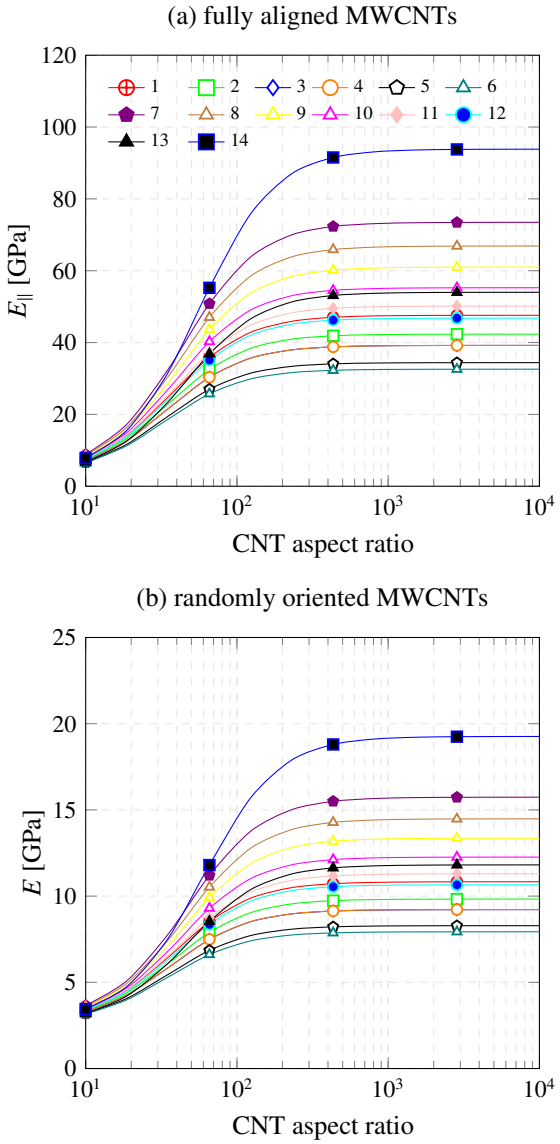

Figure 20: Variation of $E_{\|}$ with the CNT aspect ratio for PmPV doped with fully aligned MWCNTs (a) and randomly oriented MWCNTs (b) ($t = 0.10\,\text{nm}$, $f_r = 5\%$).

4. Conclusions

In this paper, a multiscale approach has been proposed for studying the elastic properties of CNT-reinforced polymer composites. Specifically, the present methodology consists of a three step bottom-up approach, including an atomistic-based continuum model, the definition of equivalent representative fibers, and a micromechanics approach. Firstly, the atomistic-based model comprises an FE cylindrical RVE that incorporates the atomic structure of a CNT, the immediately surrounding matrix, and the CNT/polymer interface. Afterwards, the cylindrical RVEs are homogenized into equivalent representative fibers that, finally, are used as inclusions within a micromechanics framework to compute the macroscopic properties of CNT/polymer composites. Two different micromechanics approaches have been used, namely the analytical Mori-Tanaka model and an FE RVE model with periodic hexagonal arrangement of fibers. On this basis, a broad range of SWCNTs and MWCNTs have been studied, as well as two different matrices. Furthermore, analytical expressions for the efficiency parameters defined in the simplified EROM have been provided. In particular, the best-fitting parameters of linear regression models have been reported for SWCNT- and MWCNT-reinforced composites and filler volume fractions up to 20 percent. Finally, detailed parametric analyses have been also presented to give insight into the sensitivity of the macroscopic properties of CNT/polymer composites to the CNT volume fraction, chirality, and aspect ratio. Overall, the main contributions of this work can be summarized as follows:

- The numerical results have evidenced the key contribution of the tube wall thickness of CNTs. On the basis of the Vodenitcharova-Zhang criterion, a tube wall thickness of 0.1 nm has been selected.
- Linear regression models have been proposed for the efficiency parameters in the EROM. The expressions comprise both SWCNT and MWCNTs, as well as PMMA and PmPV matrices for filler volume fractions up to 20 percent. Acceptable agreements have been shown between the present multiscale approach and the fitted simplified EROM.
- The sensitivity analyses have illustrated the variation of the macroscopic properties of CNT-reinforced composites with the CNT chirality, volume fraction, and aspect ratio. In the case of SWCNTs, it has been shown that zig-zag structures lead to slightly stiffer composites compared to armchair CNTs. It has been also shown that CNT aspect ratios above 1000 only yield limited increases in the macroscopic Young's modulus of the composites.

This work is envisaged to provide a valuable tool for the computational analysis of CNT-reinforced composites. The use of simplified analytical expressions, such as the EROM, is particularly helpful for preliminary analyses with very limited computational demands. On the basis of MD simulations or, as in this case, atomistic-based FEMs, it is possible to tailor simplified expressions for practical filler contents that assist preliminary design and optimization phases.

Acknowledgement

The authors gratefully acknowledge the financial support provided by the Ministerio de Economía y Competitividad of Spain under the project DPI2014-53947-R. C.F. Guzmán and E.I. Saavedra Flores acknowledge the support from the *Chilean National Commission for Scientific and Technological Research* (CONICYT), research grant FONDECYT REGULAR No.1160691, and also from the *Chilean Department of Education* (MINEDUC), grant Proyecto Fortalecimiento Usach USA1799_SE162814.

References

[1] S. Iijima, Helical microtubules of graphitic carbon, Nature 354 (1991) 56–58.

[2] R. Andrews, D. Jacques, A. M. Rao, T. Rantell, F. Derbyshire, Y. Chen, J. Chen, R. C. Haddon, Nanotube composite carbon fibers, Applied Physics Letters 75 (1999) 1329–1331.

[3] D. Qian, E. C. Dickey, R. Andrews, T. Rantell, Load transfer and deformation mechanisms in carbon nanotube-polystyrene composites, Applied physics letters 76 (2000) 2868–2870.

[4] J. N. Coleman, U. Khan, W. J. Blau, Y. K. Gun'ko, Small but strong: A review of the mechanical properties of carbon nanotube-polymer composites, Carbon 44 (2006) 1624–1652.

[5] Z. Spitalsky, D. Tasis, K. Papagelis, C. Galiotis, Carbon nanotube–polymer composites: Chemistry, processing, mechanical and electrical properties, Progress in Polymer Science 35 (2010) 357–401.

[6] T. Ebbesen, H. Lezec, H. Hiura, J. Bennett, H. Ghaemi, T. Thio, Electrical conductivity of individual carbon nanotubes, Nature 382 (1996) 54–56.

[7] B. Han, B. Han, J. Ou, Experimental study on use of nickel powder-filled portland cement-based composite for fabrication of piezoresistive sensors with high sensitivity, Sensors and Actuators A: Physical 149 (2009) 51–55.

[8] F. Ubertini, A. L. Materazzi, A. D'Alessandro, S. Laflamme, Natural frequencies identification of a reinforced concrete beam using carbon nanotube cement-based sensors, Engineering Structures 60 (2014) 265–275.

[9] B. Han, S. Ding, X. Yu, Intrinsic self-sensing concrete and structures: A review, Measurement 59 (2015) 110–128.

[10] L. Shen, J. Li, Transversely isotropic elastic properties of single-walled carbon nanotubes, Physical Review B 69 (2004) 045414.

[11] D. H. Sung, M. Kim, Y. B. Park, Prediction of thermal conductivities of carbon-containing fiber-reinforced and multiscale hybrid composites, Composites Part B: Engineering 133 (2018) 232–239.

[12] M. Rossi, M. Meo, On the estimation of mechanical properties of single-walled carbon nanotubes by using a molecular-mechanics based FE approach, Composites Science and Technology 69 (2009) 1394–1398.

[13] M. Dresselhaus, G. Dresselhaus, R. Saito, Physics of carbon nanotubes, Carbon 33 (1995) 883–891.

[14] Q. Zheng, Q. Xue, K. Yan, L. Hao, Q. Li, X. Gao, Investigation of molecular interactions between SWNT and polyethylene/polypropylene/polystyrene/polyaniline molecules, The Journal of Physical Chemistry C 111 (2007) 4628–4635.

[15] R. Rafiee, T. Rabczuk, R. Pourazizi, J. Zhao, Y. Zhang, Challenges of the modeling methods for investigating the interaction between the CNT and the surrounding polymer, Advances in Materials Science and Engineering 2013 (2013) 1–10.

[16] R. Rafiee, R. M. Moghadam, On the modeling of carbon nanotubes: A critical review, Composites Part B: Engineering 56 (2014) 435–449.

[17] V. Unnikrishnan, D. Banerjee, J. Reddy, Atomistic-mesoscale interfacial resistance based thermal analysis of carbon nanotube systems, International Journal of Thermal Sciences 47 (2008) 1602–1609.

[18] S. Frankland, The stress–strain behavior of polymer–nanotube composites from molecular dynamics simulation, Composites Science and Technology 63 (2003) 1655–1661.

[19] M. Griebel, J. Hamaekers, Molecular dynamics simulations of the elastic moduli of polymer–carbon nanotube composites, Computer Methods in Applied Mechanics and Engineering 193 (2004) 1773–1788.

[20] M. Grujicic, Y. P. Sun, K. L. Koudela, The effect of covalent functionalization of carbon nanotube reinforcements on the atomic-level mechanical properties of poly-vinyl-ester-epoxy, Applied Surface Science 253 (2007) 3009–3021.

[21] T. Chang, J. Geng, X. Guo, Prediction of chirality- and size-dependent elastic properties of single-walled carbon nanotubes via a molecular mechanics model, Proceedings of the Royal Society A: Mathematical, Physical and Engineering Sciences 462 (2006) 2523–2540.

[22] S. Meguid, J. Wernik, Z. Cheng, Atomistic-based continuum representation of the effective properties of nano-reinforced epoxies, International Journal of Solids and Structures 47 (2010) 1723–1736.

[23] A. K. Gupta, S. P. Harsha, Analysis of mechanical properties of carbon nanotube reinforced polymer composites using multi-scale finite element modeling approach, Composites Part B: Engineering 95 (2016) 172–178.

[24] J. Wernik, S. Meguid, Multiscale micromechanical modeling of the constitutive response of carbon nanotube-reinforced structural adhesives, International Journal of Solids and Structures 51 (2014) 2575–2589.

[25] S. J. V. Frankland, A. Caglar, D. W. Brenner, M. Griebel, Molecular simulation of the influence of chemical cross-links on the shear strength of carbon nanotube polymer interfaces, The Journal of Physical Chemistry B 106 (2002) 3046–3048.

[26] M. M. Shokrieh, R. Rafiee, On the tensile behavior of an embedded carbon nanotube in polymer matrix with non-bonded interphase region, Composite Structures 92 (2010) 647–652.

[27] S. Yang, S. Yu, W. Kyoung, D. S. Han, M. Cho, Multiscale modeling of size-dependent elastic properties of carbon nanotube/polymer nanocomposites with interfacial imperfections, Polymer 53 (2012) 623–633.

[28] Z. Lei, L. Zhang, K. Liew, Parametric analysis of frequency of rotating laminated CNT reinforced functionally graded cylindrical panels, Composites Part B: Engineering 90 (2016) 251–266.

[29] L. Zhang, L. Xiao, G. Zou, K. Liew, Elastodynamic analysis of quadrilateral CNT-reinforced functionally graded composite plates using FSDT element-free method, Composite Structures 148 (2016) 144–154.

[30] L. W. Zhang, Y. Zhang, G. L. Zou, K. M. Liew, Free vibration analysis of triangular CNT-reinforced composite plates subjected to in-plane stresses using FSDT element-free method, Composite Structures 149 (2016) 247–260.

[31] E. García-Macías, R. Castro-Triguero, E. I. S. Flores, M. I. Friswell, R. Gallego, Static and free vibration analysis of functionally graded carbon nanotube reinforced skew plates, Composite Structures (2016).

[32] Y. Kiani, Thermal post-buckling of FG-CNT reinforced composite plates, Composite Structures 159 (2017) 299–306.

[33] H. S. Shen, Nonlinear bending of functionally graded carbon nanotube-reinforced composite plates in thermal environments, Composite Structures 91 (2009) 9–19.

[34] C. Li, T. W. Chou, A structural mechanics approach for the analysis of carbon nanotubes, International Journal of Solids and Structures 40 (2003) 2487–2499.

[35] A. K. Rappe, C. J. Casewit, K. S. Colwell, W. A. Goddard, W. M. Skiff, UFF, a full periodic table force field for molecular mechanics and molecular dynamics simulations, Journal of the American chemical society 114 (1992) 10024–10035.

[36] Y. Jin, F. G. Yuan, Elastic Properties of Single-Walled Carbon Nanotubes, American Institute of Aeronautics and Astronautics, Reston, Virigina, 2002.

[37] N. Hu, H. Fukunaga, C. Lu, M. Kameyama, B. Yan, Prediction of elastic properties of carbon nanotube reinforced composites, in: Proceedings of the Royal Society of London A: Mathematical, Physical and Engineering Sciences, volume 461, 2005, pp. 1685–1710.

[38] ANSYS® Academic Research, Release 16.1, 2015.

[39] J. E. Lennard-Jones, On the determination of molecular fields. II. From the equation of state of a gas, Proceedings of the Royal Society of London A: Mathematical, Physical and Engineering Sciences 106 (1924) 463–477.

[40] C. W. Fan, Y. Y. Liu, C. Hwu, Finite element simulation for estimating the mechanical properties of multi-walled carbon nanotubes, Applied Physics A: Materials Science & Processing 95 (2009) 819–831.

[41] R. Hill, A self-consistent mechanics of composite materials, Journal of the Mechanics and Physics of Solids 13 (1965) 213–222.

[42] F. Tornabene, M. Bacciocchi, N. Fantuzzi, J. N. Reddy, Multiscale approach for three-phase cnt/polymer/fiber laminated nanocomposite structures, Polymer Composites. In press (2017). doi:10.1002/pc.24520.

[43] T. Mori, K. Tanaka, Average stress in matrix and average elastic energy of materials with misfitting inclusions, Acta metallurgica 21 (1973) 571–574.

[44] J. D. Eshelby, The determination of the elastic field of an ellipsoidal inclusion, and related problems, in: Proceedings of the Royal Society of London A: Mathematical, Physical and Engineering Sciences, volume 241, 1957, pp. 376–396.

[45] T. Mura, Micromechanics of defects in solids, volume 3, Springer, 1987.

[46] Y. Benveniste, A new approach to the application of Mori-Tanaka's theory in composite materials, Mechanics of materials 6 (1987) 147–157.

[47] M. A. Van Es, Polymer-clay nanocomposites: the importance of particle dimensions, Ph.D. thesis, Delft, The Netherlands: Delft University of Technology, 2001.

[48] E. J. Barbero, Finite element analysis of composite materials using ANSYS®, CRC press, 2013.

[49] J. Schjødt-Thomsen, R. Pyrz, The Mori-Tanaka stiffness tensor: diagonal symmetry, complex fibre orientations and non-dilute volume fractions, Mechanics of Materials 33 (2001) 531–544.

[50] M. Meo, M. Rossi, Tensile failure prediction of single wall carbon nanotube, Engineering Fracture Mechanics 73 (2006) 2589–2599.

[51] J. Doh, J. Lee, Prediction of the mechanical behavior of double walled-CNTs using a molecular mechanics-based finite element method: Effects of chirality, Computers & Structures 169 (2016) 91–100.

[52] E. Mohammadpour, M. Awang, Predicting the nonlinear tensile behavior of carbon nanotubes using finite element simulation, Applied Physics A: Materials Science & Processing 104 (2011) 609–614.

[53] T. Belytschko, S. P. Xiao, G. C. Schatz, R. S. Ruoff, Atomistic simulations of nanotube fracture, Physical Review B 65 (2002) 235430.

[54] P. M. Morse, Diatomic Molecules According to the Wave Mechanics. II. Vibrational Levels, Physical Review 34 (1929) 57–64.

[55] T. Natsuki, M. Endo, Stress simulation of carbon nanotubes in tension and compression, Carbon 42 (2004) 2147–2151.

[56] T. Chang, H. Gao, Size-dependent elastic properties of a single-walled carbon nanotube via a molecular mechanics model, Journal of the Mechanics and Physics of Solids 51 (2003) 1059–1074.

[57] J. Xiao, J. Staniszewski, J. Gillespie, Fracture and progressive failure of defective graphene sheets and carbon nanotubes, Composite Structures 88 (2009) 602–609.

[58] C. Li, T. W. Chou, Elastic moduli of multi-walled carbon nanotubes and the effect of van der Waals forces, Composites Science and Technology 63 (2003) 1517–1524.

[59] C. Y. Wang, L. C. Zhang, A critical assessment of the elastic properties and effective wall thickness of single-walled carbon nanotubes, Nanotechnology 19 (2008) 075705.

[60] T. Vodenitcharova, L. C. Zhang, Effective wall thickness of a single-walled carbon nanotube, Physical Review B 68 (2003) 165401.

[61] A. Allaoui, S. Bai, H. M. Cheng, J. Bai, Mechanical and electrical properties of a MWNT/epoxy composite, Composites Science and Technology 62 (2002) 1993–1998.

[62] F. Tornabene, N. Fantuzzi, M. Bacciocchi, E. Viola, Effect of agglomeration on the natural frequencies of functionally graded carbon nanotube-reinforced laminated composite doubly-curved shells, Composites Part B: Engineering 89 (2016) 187–218.

[63] D. Banić, M. Bacciocchi, F. Tornabene, A. J. M. Ferreira, Influence of winkler-pasternak foundation on the vibrational behavior of plates and shells reinforced by agglomerated carbon nanotubes, Applied Sciences 7 (2017) 1228.

[64] X. Lei, T. Natsuki, J. Shi, Q. Q. Ni, Analysis of carbon nanotubes on the mechanical properties at atomic scale, Journal of Nanomaterials 2011 (2011) 1–10.